J. Fluid Mech. (2024), *vol*. 981, A5, doi:10.1017/jfm.2024.14

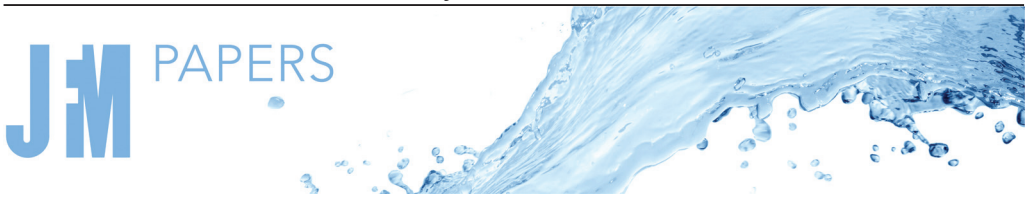

Effects of dilatation and turbulence on tangential strain rates in premixed hydrogen and iso-octane flames

Hongchao Chu[1],†, **Lukas Berger**[1], **Michael Gauding**[1], **Antonio Attili**[2] and **Heinz Pitsch**[1]

[1]Institute for Combustion Technology, RWTH Aachen University, 52056 Aachen, Germany

[2]Institute for Multiscale Thermofluids, School of Engineering, University of Edinburgh, Edinburgh EH9 3FD, UK

(Received 14 June 2023; revised 16 November 2023; accepted 26 December 2023)

The tangential strain rate in premixed flames impacts significantly the flame surface area generation and thus the combustion process. Studies on incompressible isotropic turbulence have revealed that the mean tangential strain rate at material and iso-scalar surfaces is positive and exhibits a universal value when normalized by the Kolmogorov time. This is associated with the preferential alignment of the surface normal with the most compressive principal strain rate. The present study investigates such effects in premixed hydrogen and iso-octane flame kernels using direct numerical simulations. It is shown that the normalized mean tangential strain rate of the investigated flames has a very similar value compared with the incompressible flows. However, in the reaction zone, the flame surface normal aligns preferentially with the most extensive principal strain rate. Furthermore, this alignment depends on the reaction progress variable and the Lewis number, while the tangential strain rate remains independent of these parameters. Such counter-intuitive behaviour is systematically investigated by decomposing the effects of dilatation and residual solenoidal turbulence. It is found that the solenoidal turbulence influences significantly the tangential strain rate. A general effect of turbulence on the tangential strain rate is identified, which is consistent with incompressible flows and independent of the Lewis number and the reaction progress variable. This is a remarkable finding indicating that models of the tangential strain rate developed based on incompressible flows apply also to premixed flames with different Lewis numbers, and, for the modelling, only the solenoidal turbulence should be considered.

Key words: combustion, turbulent reacting flows

† Email address for correspondence: h.chu@itv.rwth-aachen.de

1. Introduction

For premixed flames, turbulence impacts the combustion process mainly through two mechanisms: (i) the flame surface area evolution and (ii) the local flame propagation speed (Bray 1990; Bray & Libby 1994; Peters 2001). The evolution of an element of flame surface area δA can be described by the flame stretch rate

$$K = \frac{1}{\delta A}\frac{\mathrm{d}\delta A}{\mathrm{d}\tau}, \tag{1.1}$$

which can be written as follows (Candel & Poinsot 1990):

$$K = s_d\kappa + a_t. \tag{1.2}$$

It contains two components: $s_d\kappa$ accounts for the surface area change due to the flame propagation in the presence of curvature κ. Positive curvatures refer to convexly curved flame segments towards the unburned gas. The displacement speed, s_d, describes the relative motion of the flame surface to the flow field. The tangential strain rate, a_t, describes the influence of the flow on the evolution of the flame surface area and can be expressed as

$$a_t = \Delta - \boldsymbol{nn} : \nabla \boldsymbol{u}, \tag{1.3}$$

where $\Delta = \nabla \cdot \boldsymbol{u}$ is the dilatation rate, $\boldsymbol{n}$ is the unit surface normal vector pointing towards the unburned gas and $\boldsymbol{u}$ is the flow velocity.

The impact of tangential strain rate on the evolution of material and propagating surfaces in incompressible flows and turbulent premixed flames has received considerable interest (Ashurst *et al.* 1987; Girimaji & Pope 1990; Yeung, Girimaji & Pope 1990; Girimaji & Pope 1992; Rutland & Trouvé 1993; Chakraborty & Swaminathan 2007; Kim & Pitsch 2007; Sankaran *et al.* 2007, 2015; Chakraborty, Klein & Swaminathan 2009; Hawkes *et al.* 2012; Dopazo *et al.* 2015; Wang, Hawkes & Chen 2016; Wang *et al.* 2017; Luca *et al.* 2019; Krisman *et al.* 2021; Kulkarni & Bisetti 2021; Berger, Attili & Pitsch 2022; Gauding *et al.* 2022). Yeung *et al.* (1990) investigated the straining of material surfaces in incompressible turbulence and found that the alignment of the surface normal with the principal strain rates plays a vital role for the average tangential strain rate at the surfaces. The tangential strain rate can be written as

$$a_t = \Delta - \left(\lambda_1 \cos^2\varphi_1 + \lambda_2 \cos^2\varphi_2 + \lambda_3 \cos^2\varphi_3\right), \tag{1.4}$$

where λ_i denotes the eigenvalues of the strain rate tensor ($\lambda_1 \geq \lambda_2 \geq \lambda_3$, $\lambda_1 + \lambda_2 + \lambda_3 = \Delta$), and φ_i is the angle between the surface normal and the principal strain rates, whose direction is given by the eigenvectors of the strain rate tensor. For incompressible flows,

$$\Delta = \lambda_1 + \lambda_2 + \lambda_3 = 0 \quad \text{and} \quad \lambda_1 > 0 > \lambda_3. \tag{1.5a,b}$$

If the surface normal aligns with the most compressive principal strain rate,

$$\cos^2\varphi_1 = \cos^2\varphi_2 = 0 \quad \text{and} \quad \cos^2\varphi_3 = 1. \tag{1.6a,b}$$

According to (1.4), a positive tangential strain rate is obtained: $a_t = 0 - \lambda_3 > 0$. Similarly, if the surface normal aligns with the most extensive principal strain rate, the tangential strain rate is negative: $a_t = 0 - \lambda_1 < 0$. Yeung *et al.* (1990) found that the normal of the material surface aligns preferentially with the most compressive principal strain rate, which results in a positive surface-averaged normalized tangential strain rate of $\tau_\eta\langle a_t\rangle_s = 0.28$, where τ_η is the Kolmogorov time. The operator $\langle\cdot\rangle_s$ denotes the surface average. It is

worth noting that a_t of a randomly oriented surface in incompressible isotropic turbulence has a zero mean. Girimaji & Pope (1990) and Gauding *et al.* (2022) demonstrated that the value 0.28 holds valid in incompressible turbulence for a wide range of Reynolds and Schmidt numbers. In turbulent premixed flames, similar values of $\tau_\eta\langle a_t\rangle_s$ have been reported for various configurations by different authors using simplified Arrhenius one-step and detailed chemistry models, with and without the constant density assumption (Rutland & Trouvé 1993; Luca *et al.* 2019; Kulkarni & Bisetti 2021; Berger *et al.* 2022). However, Chakraborty *et al.* (2009) and Kim & Pitsch (2007) found that the flame surface normal can align preferentially with the most extensive principal strain rate in the reaction zone due to the dilatation from heat release. They did not evaluate the value of $\tau_\eta\langle a_t\rangle_s$, while Chakraborty *et al.* (2009) showed that the mean value of a_t is positive. Therefore, it is not yet clear whether the specific value of $\tau_\eta\langle a_t\rangle_s \approx 0.28$ is also obtained for premixed flames when the flame surface normal aligns preferentially with the most extensive principal strain rate, and whether this varies for different combustion regimes. Further, the dependence of this alignment on the Lewis number and the value of the reaction progress variable used to define the flame surface appears to contradict the independence of the tangential strain rate on these parameters. Rutland & Trouvé (1993) found that $\tau_\eta\langle a_t\rangle_s = 0.28$ holds for premixed flames with different Lewis numbers from 0.8 to 1.2. Dopazo *et al.* (2015) and Berger *et al.* (2022) showed that the averaged tangential strain rate is almost constant for different iso-surfaces of the reaction progress variable. Chakraborty *et al.* (2009) also reported that the distributions of the tangential strain rate are similar for different iso-surfaces of the reaction progress variable and different Lewis numbers (0.34 to 1.2). However, they found that the alignment of the flame surface normal with the principal strain rates depends strongly on the Lewis numbers and the reaction progress variable.

The positive straining of material surfaces in incompressible flows ($\tau_\eta\langle a_t\rangle_s = 0.28$) results from the preferential alignment of the surface normals with the most compressive principal strain rates (Yeung *et al.* 1990). Despite the differences in the alignment characteristics between flames and incompressible flows, coefficients and scaling law in the current models of the tangential strain rate on flame surfaces usually originate from studies on incompressible flows (Cant, Pope & Bray 1991; Duclos, Veynante & Poinsot 1993; Hawkes & Cant 2001; Chakraborty 2021) with Reynolds-averaged quantities replaced by Favre-averaged quantities. A particular example is the flame surface density (FSD) approach, where the sub-grid tangential strain rate in the transport equation of FSD is often modelled by using the Kolmogorov time scale as $0.28(\tilde{\epsilon}/\nu_0)^{1/2}$, where $\tilde{\epsilon}$ is the Favre-averaged dissipation rate and ν_0 is the unburned-gas kinematic viscosity (Cant *et al.* 1991; Chakraborty 2021). A better understanding of the effects of heat release, dilatation, and their interactions with turbulence on the tangential strain rate and the alignment of the flame surface normal with the principal strain rates in premixed flames will shed more light on the modelling of turbulent premixed combustion. The first objective of the current work is to investigate these effects by introducing a decomposition approach to separately consider the effects of combustion, namely dilatation, and the residual solenoidal turbulence in premixed flames. It is hypothesized that the solenoidal part of the turbulence in premixed flames governs the tangential strain rate and has the same effects as in incompressible flows.

The second objective of the current work is to assess the local effects of the small-scale turbulence on the local tangential strain rate, which is of importance for the early development of flame kernels in spark-ignition (SI) internal combustion engines (ICEs) (Chu *et al.* 2023*a*). The variations of such early flame kernel development influence significantly the cycle-to-cycle variations (CCVs) in SI ICEs (Young 1981; Schiffmann,

Reuss & Sick 2018; Zeng *et al.* 2019; Chu *et al.* 2022), and thus are of practical importance for the design and optimization of such engines (Aleiferis *et al.* 2004; Fontana & Galloni 2010; Jung, Sasaki & Iida 2017; Karvountzis-Kontakiotis *et al.* 2017; Luszcz *et al.* 2018; Kargul *et al.* 2019; Ye *et al.* 2021). In an SI ICE, the initial flame kernel ignited by a spark is typically smaller than the size of the turbulent integral length scales (Falkenstein *et al.* 2020*a*). The evolution of such small flame kernels is dominated by local, intermittent flow fluctuations, which are not well represented by their ensemble average and thus can vary under the same nominal conditions. Therefore, it is of practical interest to assess the effects of the local small-scale turbulence on the local tangential strain rate.

For these purposes, the DNS database (Chu *et al.* 2023*a*) of hydrogen and iso-octane flame kernels under engine conditions with significantly different Lewis numbers and turbulence-flame interactions is analysed. The paper is organized in the following manner. First, a brief description of the DNS database is provided. Then, the analysis results are presented and discussed, including an approach for separating the effects of solenoidal turbulence and dilatation on the tangential strain rate in premixed flames. Finally, the paper finishes with conclusions.

2. DNS database

2.1. *Configuration*

In this study, the DNS database by Chu *et al.* (2023*a*) and Falkenstein *et al.* (2020*a*) consisting of multiple realizations of premixed hydrogen and iso-octane flame kernels under engine conditions with significantly different Lewis numbers is considered. The flame kernels were ignited in a decaying homogeneous isotropic turbulent (HIT) field of homogeneous fuel–air mixtures. The HIT field is initialized using the same method as Kulkarni *et al.* (2021). The thermodynamic parameters were specified to represent part load operation conditions of gasoline SI engines (Falkenstein *et al.* 2020*a*) and medium load conditions of hydrogen engines (Tang *et al.* 2002; Verhelst *et al.* 2009; Jilakara *et al.* 2015). The volumetric energy density ratio of the hydrogen mixture to the iso-octane mixture is approximately 2 : 1. The flow parameters, such as turbulent Reynolds number Re_t, Karlovitz number Ka and Damköhler number Da, were specified as closely as possible to typical SI engine conditions, which can be found from Falkenstein *et al.* (2020*a*). The characteristic numbers of the DNS are listed in table 1. Flames for both fuels fall into the thin reaction zones regime of premixed turbulent combustion. Multiple realizations of turbulent flame kernels were simulated for both fuels by placing the ignition source at different locations in the same initial turbulent flow field. Ignition was realized by a heat source varying smoothly in time and space as used by Falkenstein *et al.* (2020*a*). The ignition energy was specified as 1.4 times the minimum ignition energy, which was determined in a quiescent environment and different in the two mixtures, to ensure successful ignition in the turbulent fields (Falkenstein *et al.* 2020*a*; Chu *et al.* 2023*b*). For a detailed description of the DNS database including the specification of the ignition locations for different realizations, the readers are referred to Chu *et al.* (2023*a*). In this study, the fastest and the slowest flame kernels for each fuel are considered, which exhibit significantly different kernel growth rates and tangential strain rates. It is worth noting that in this study, the configuration of developing flame kernels is considered because the tangential strain rate of very early flame kernels has tremendous practical interest as it was found to significantly influence the growth rate of the kernels (Chu *et al.* 2023*a*), which has leading order effect on the cycle-to-cycle variations of SI engines. The main findings

Case name	iso-C_8H_{18}	H_2
Flow field	HIT	HIT
Re_t	385	385
Re_λ	76	76
u'/s_l^0	5.9	6.6
Ka	10.6	8.5
Da	1.9	2.3
l_t/l_η	87	87
l_λ/l_η	17	17
l_t/l_f^0	10.9	15.1
Domain length	$15l_t$	$10l_t$
Grid size	960^3	1440^3
$l_\eta/\Delta x$	0.7	1.7
Mixture	Iso-octane–air	Hydrogen–air
p (bar)	6	40
T_u (K)	600	800
ϕ	1.0	0.4
Le_{eff}	2.0	0.3
s_l^0 (m s^{-1})	0.73	0.44
l_f^0 (μm)	69	20
R_{ign}/l_t	0.38	0.33

Table 1. Conditions and characteristic numbers of DNS: turbulent Reynolds number $Re_t = l_t u'/\nu$, root mean square of the turbulent velocity fluctuations u', turbulent integral length scale $l_t = u'^3/\bar{\epsilon}$, mean dissipation rate $\bar{\epsilon}$, kinematic viscosity ν, Reynolds number based on Taylor length scale $Re_\lambda = l_\lambda u'/\nu$, Taylor length scale $l_\lambda = (15\nu u'^2/\bar{\epsilon})^{1/2}$, unstretched laminar flame speed s_l^0, Karlovitz number $Ka = \tau_f^0/\tau_\eta$, Damköhler number $Da = \tau_t/\tau_f^0$, chemical time $\tau_f^0 = l_f^0/s_l^0$, Kolmogorov time $\tau_\eta = (\nu/\bar{\epsilon})^{1/2}$, turbulent integral time $\tau_t = l_t/u'$, unstretched laminar flame thickness computed from the maximum temperature gradient l_f^0, Kolmogorov length l_η, cell size Δx, initial pressure p and temperature T_u, fuel/air equivalence ratio ϕ, effective Lewis number evaluated according to Joulin & Mitani (1981) Le_{eff}, and ignition radius R_{ign}.

discussed in this study remain unchanged when a planar turbulent flame is considered, which is shown in Appendix B.

2.2. *Governing equations and numerical methods*

The reacting flow has been modelled in the low-Mach limit (Müller 1998), and chemical reactions have been described for hydrogen and iso-octane combustion with a detailed mechanism proposed by Konnov (2019) and a modified model (Falkenstein *et al.* 2020*a*) based on the skeletal iso-octane mechanism by Pitsch, Peters & Seshadri (1996), respectively. The two mechanisms have been validated with experiments under different conditions. The diffusive scalar transport has been modelled with the Curtiss–Hirschfelder approximation (Hirschfelder *et al.* 1964). The diffusion coefficients have been determined by setting the species Lewis numbers constant and computing them in the burned gas of the corresponding unstretched laminar flames. The Soret effect has been included following Zhou *et al.* (2017) and Schlup & Blanquart (2018) with a mixture-averaged thermal diffusion model. The ideal gas law has been applied as the equation of state. The DNS has been carried out with a semi-implicit finite difference code based on the Crank–Nicolson time advancement scheme and an iterative predictor-corrector scheme with spatial and temporal staggering (Desjardins *et al.* 2008). The Poisson equation for the pressure correction has been solved by the multi-grid HYPRE solver (Falgout &

Yang 2002). Second-order central difference schemes have been employed for momentum convection and all diffusive fluxes, while a fifth-order weighted essentially non-oscillatory (WENO) (Jiang & Shu 1996) scheme has been applied for scalar convection to ensure bounded solutions. For species and temperature, the operator splitting proposed by Strang (1968) has been used. The resulting ordinary differential equation for chemical source terms has been solved using the CVODE solver from the SUNDIALS package (Hindmarsh *et al.* 2005).

3. Results and discussion

To analyse premixed flames, it is useful to define a reaction progress variable. In this study, the reaction progress variable C of the hydrogen flame kernels is defined using the mass fraction of molecular hydrogen $Y_{\mathrm{H_2}}$, as suggested by Berger *et al.* (2022),

$$C = 1 - Y_{\mathrm{H_2}}/Y_{\mathrm{H_{2,}u}}, \tag{3.1}$$

where $Y_{\mathrm{H_{2,}u}}$ is the hydrogen mass fraction in the unburned gas mixture. For the iso-octane flame kernels, as in the studies by Falkenstein *et al.* (2020*b*) and Chu *et al.* (2023*a*), a reaction progress variable C is defined by the solution of the transport equation

$$\rho\frac{\partial C}{\partial \tau} + \rho\boldsymbol{u}\cdot\boldsymbol{\nabla} C = \dot{\omega}_C''' + \boldsymbol{\nabla}\cdot(\rho D_{th}\boldsymbol{\nabla} C)\,, \tag{3.2}$$

where $D_{th} = \lambda/(\rho c_p)$ denotes the thermal diffusivity, λ the thermal conductivity, ρ the density and c_p the specific heat capacity. The chemical source term $\dot{\omega}_C'''$ is defined based on the major product species,

$$\dot{\omega}_C''' = \dot{\omega}_{\mathrm{H_2}}''' + \dot{\omega}_{\mathrm{H_2O}}''' + \dot{\omega}_{\mathrm{CO}}''' + \dot{\omega}_{\mathrm{CO_2}}'''. \tag{3.3}$$

Equation (3.2) exhibits a simplified diffusion term without differential diffusion. In the DNS, the passive scalar C is solved solely for post-processing, which does not influence the simulation results, however, simplifies significantly the analysis of premixed flames (Falkenstein *et al.* 2020*b*). Falkenstein *et al.* (2020*b*) have shown that this simplification has negligible influence under the investigated conditions. This progress variable definition is used so that the analysis in this study is consistent with our previous studies (Falkenstein *et al.* 2020*b*; Chu *et al.* 2023*a*). Using other progress variable definitions, such as $C = Y_{\mathrm{CO_2}}$, does not change the main findings in this study. Results using $C = Y_{\mathrm{CO_2}}$ are provided in Appendix B. The flame surface can be defined as an iso-surface of C. The surface average of a quantity Q on the surface of $C = C_0$ is given as

$$\langle Q\rangle_{s,C_0} = \frac{\int Q\,|\boldsymbol{\nabla} C|\,\delta\,(C - C_0)\,\mathrm{d}V}{\int |\boldsymbol{\nabla} C|\,\delta\,(C - C_0)\,\mathrm{d}V}, \tag{3.4}$$

where δ is the Dirac delta function. In premixed combustion, quantities may vary for different iso-surfaces of C. The average behaviour of a quantity Q considering all iso-surfaces of C can be described by the generalized iso-surface average

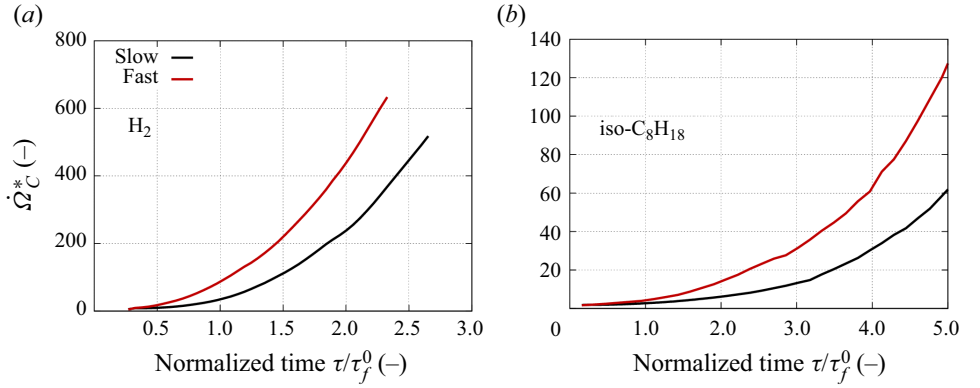

Figure 1. Normalized integrated reaction progress variable source term as a function of normalized time (Chu *et al.* 2023*a*): (*a*) hydrogen and (*b*) iso-octane.

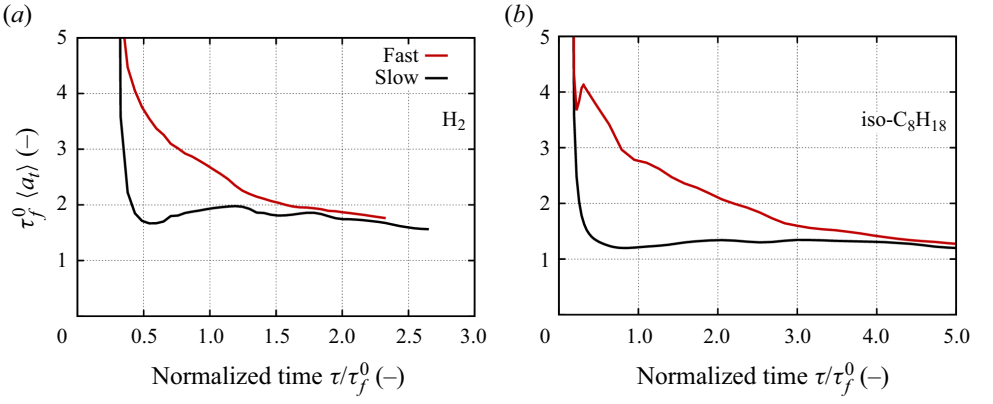

Figure 2. Generalized iso-surface average of the tangential strain rate as a function of time (Chu *et al.* 2023*a*). The variables are normalized with the chemical time τ_f^0. (*a*) Hydrogen and (*b*) iso-octane.

(Boger *et al.* 1998), which is given by

$$\langle Q \rangle = \frac{\int Q\,|\nabla C|\,\mathrm{d}V}{\int |\nabla C|\,\mathrm{d}V}. \tag{3.5}$$

In this study, two flame kernel realizations are considered for each fuel. Figure 1 shows the evolution of the fuel consumption rate, which is expressed as the normalized integrated reaction progress variable source term, $\dot{\Omega}_C^* = \int \dot{\omega}_C\,\mathrm{d}V/(\rho_u s_l^0 A_{ref} C_{max})$. Here, $A_{ref} = 4\pi R_{ign}$ is a normalization constant. Significant differences in the fuel consumption rate between the two realizations are observed for each fuel. Realizations that exhibit the larger (or smaller) fuel consumption rate are referred to as 'fast' (or 'slow') kernels. Such difference in the fuel consumption rate for each fuel is attributed to the various tangential strain rates of different realizations, which are shown in figure 2. A comprehensive discussion of the impact of tangential strain rate on the fuel consumption rate can be found from Chu *et al.* (2023*a*). In figure 2, the generalized iso-surface average of the tangential strain rate is presented, as it directly influences the fuel consumption rate (Chu *et al.*

2023*a*). Quantities are normalized by the chemical time $\tau_f^0 = l_f^0/s_l^0$, which is the same for the fast and slow kernels of each fuel (table 1). The initial high values are due to ignition. Different realizations of both fuels exhibit substantial variations in tangential strain rates shortly after ignition. This originates from the different flow conditions around the ignition locations. A trend towards the same value is observed in both fuels as the kernels grow since the homogeneous statistical behaviour of the flame-turbulence interactions in HIT is expected for spherical flames of sizes much larger than the turbulent integral length scale. In the following, the tangential strain rates of both fuels at various times are examined. Specifically, the analysis will focus on time instances at $\tau = 0.5\tau_f^0$ for both fuels with large a_t differences between the fast and the slow flame kernels, as well as $\tau = 2\tau_f^0$ for hydrogen and $\tau = 4\tau_f^0$ for iso-octane with small differences of a_t. An illustration of the selected eight cases is provided in figure 3. Significant differences among the cases can be identified, for example, the flame kernel topology, the surface wrinkling, the size of the flame kernels compared with the turbulent integral length, and the distribution of the heat release rate in positively and negatively curved regions. Such database makes possible a direct test of the proposed hypothesis. A general behaviour of the tangential strain rate and the alignment of the strain rate tensor with the surface is hypothesized for all the cases after decomposition. For a detailed comparison of the different cases and the explanation for the difference, the readers are referred to our previous studies (Chu *et al.* 2023*a*, 2023*b*).

3.1. *Tangential strain rate and dilatation rate*

Figure 4 shows the surface averaged tangential strain rate $\langle a_t \rangle_{s,C}$ and dilatation rate $\langle \Delta \rangle_{s,C}$ as functions of the reaction progress variable C. The tangential strain rate has been normalized with the Kolmogorov time evaluated in the unburned mixture ($C \approx 0.01$), $\tau_\eta = (\nu/\bar{\epsilon})^{1/2}$, using the average dissipation rate in the unburned mixture, $\bar{\epsilon}$. It is worth noting that τ_η is different for different cases. In particular, for each fuel at $0.5\tau_f^0$, τ_η of the fast and the slow kernels are significantly different. The dilatation rate has been normalized with both the Kolmogorov time τ_η and the chemical time τ_f^0 which is a constant for each fuel. As a reference, the joint probability density functions (j.p.d.f.s) for the fast kernel at the later time, $2\tau_f^0$ for hydrogen and $4\tau_f^0$ for iso-octane, are also displayed. As expected, the flame heat release causes positive dilatation rates in the reaction zone. At $0.5\tau_f^0$, the ignition heat source is still affecting the flame as shown by the increased normalized dilatation rate $\tau_f^0\Delta$ compared with the later time for both fuels. The dilatation rate normalized with the Kolmogorov time $\tau_\eta\Delta$ describes its relative strength compared with small-scale turbulence, which is different for fast and slow kernels. In contrast to the dependence of the dilatation rate on the progress variable, the tangential strain rate is almost constant across the flame for both fuels, which is consistent with the results of Dopazo *et al.* (2015) and Berger *et al.* (2022). Even though the value of the absolute tangential strain rate at $0.5\tau_f^0$ of the fast kernel is approximately twice as large as the slow kernel for both fuels (figure 2) and the flames at $0.5\tau_f^0$ exhibit stronger dilatation rates due to the ignition heat source, the tangential strain rate normalized with the Kolmogorov time scale is almost the same and close to the value of $\tau_\eta\langle a_t \rangle_s \approx 0.28$ for all cases. Similar values of $\tau_\eta\langle a_t \rangle_s$ have also been reported by different authors for various configurations and fuels: planar premixed flames in HIT with single-step Arrhenius kinetics chemistry and constant density by Rutland & Trouvé (1993), premixed methane–air jet flames with detailed chemistry by Luca *et al.* (2019), spherically expanding premixed methane–air

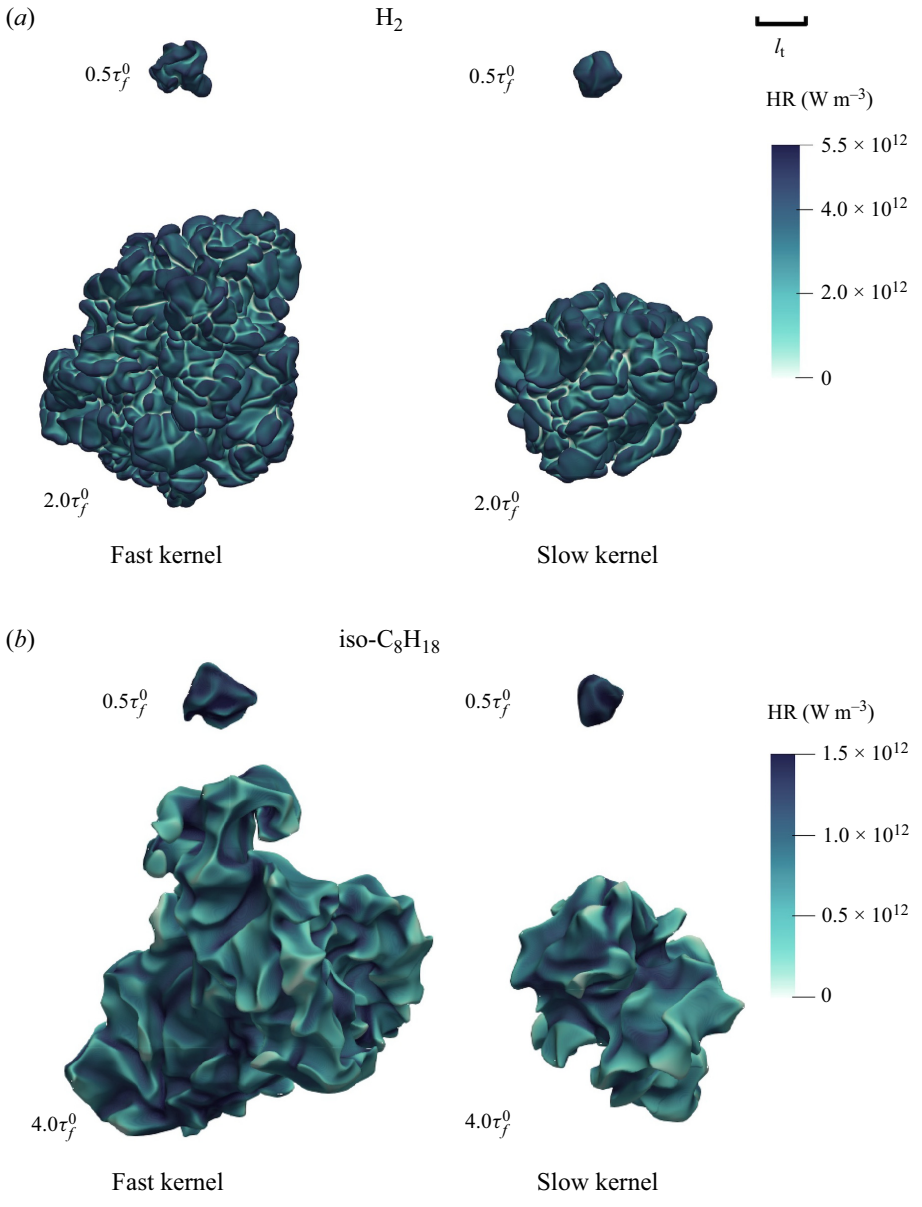

Figure 3. Illustration of the selected eight cases: iso-surface of progress variable corresponding to maximum heat release (in an unstretched flame) coloured with heat release rate (Chu *et al.* 2023*a*). For the sake of comparability, the size of the kernels is rescaled so that the turbulent integral length l_t for both fuels has the same length in the figure, which is displayed on the top right.

flames in HIT with detailed chemistry by Kulkarni & Bisetti (2021), and premixed hydrogen–air jet flame with detailed chemistry by Berger *et al.* (2022). Moreover, Kulkarni & Bisetti (2021) demonstrated that the normalized tangential strain rate is independent of the Reynolds number in the range of $Re_\lambda = 44$–77 and the Karlovitz number in the range of $Ka = 25$–59. It is worth noting that this value is also in very good agreement with the study by Yeung *et al.* (1990), who investigated the strained material surfaces in incompressible isotropic turbulence. The reason why the tangential strain rate of premixed

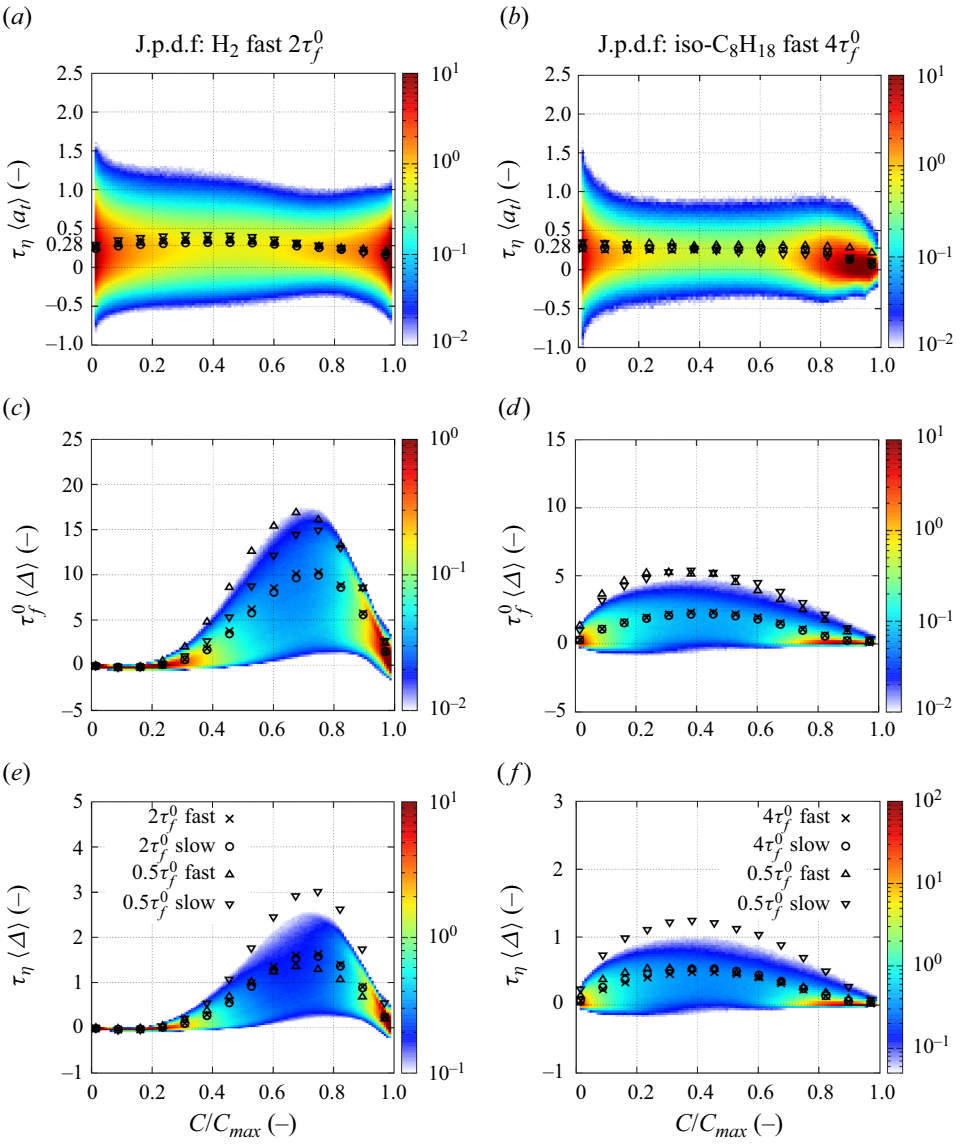

Figure 4. Normalized tangential strain rate $\tau_\eta\langle a_t\rangle$, and dilatation rate $\tau_f^0\langle\Delta\rangle$ and $\tau_\eta\langle\Delta\rangle$ as functions of C. The variables are normalized with the chemical time τ_f^0 or the Kolmogorov time, τ_η, evaluated in the unburned mixture. (*a*,*c*,*e*) Hydrogen and (*b*,*d*,*f*) iso-octane. The colour maps represent the j.p.d.f. of the fast kernels at $2\tau_f^0$ for hydrogen and $4\tau_f^0$ for iso-octane.

flames has the same value as material surfaces in incompressible flows and under which conditions this holds valid are discussed in the following sections.

3.2. *Alignment of the flame normal with the principal strain rates*

The value of $\tau_\eta\langle a_t\rangle_s \approx 0.28$ for material surfaces in incompressible flows results from the persistent straining of the surfaces due to the preferential alignment of the surface normal with the most compressive principal strain rates. In this section, such alignment characteristics in the premixed hydrogen and iso-octane flame kernels are assessed.

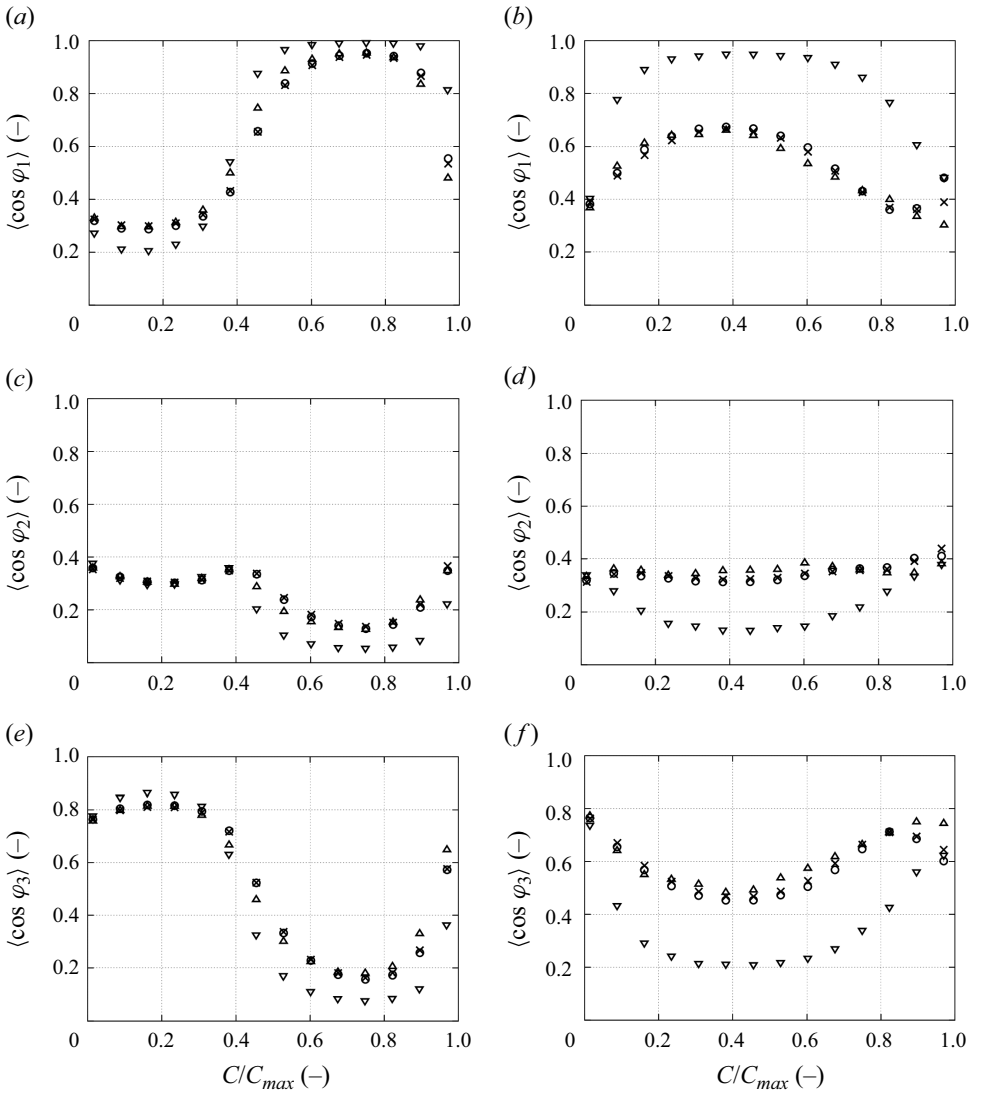

Figure 5. Alignment characteristics between the principal strain rates and the iso-surfaces of C, expressed by $\cos\varphi_i$, as a function of C. Symbols represent the conditional surface average for different cases as given in figure 4. (*a*,*c*,*e*) Hydrogen and (*b*,*d*,*f*) iso-octane.

Figure 5 shows the surface averaged alignment characteristics of the strain rate tensor and the normal vector of the iso-surfaces of C as functions of C. The strain rate tensor and the normal vector are computed independently for each iso-surface of C. The alignment characteristics are expressed by the term $\cos\varphi_i$ (cf. (1.4)) with $\cos^2\varphi_1 + \cos^2\varphi_2 + \cos^2\varphi_3 = 1$. The probability density functions (p.d.f.s) of $\cos\varphi_i$ for the fast kernels at the later time, $2\tau_f^0$ for hydrogen and $4\tau_f^0$ for iso-octane, are provided in Appendix A (figure 18). Here, $\cos\varphi_i$ varies across the flame and exhibits different behaviours for different cases (cf. the surface average in figure 5). This is consistent with the previous findings by Chakraborty *et al.* (2009), who showed that the alignment characteristics of the flame surface normal with the principal strain rates are significantly

influenced by the Lewis number and the value of the reaction progress variable used to define the flame surface. The dependence of the alignment characteristics on the reaction progress variable was also reported by Kim & Pitsch (2007). According to figures 4 and 5, it can be concluded that for regions with low dilatation rates, the normals of the iso-surfaces of C align preferentially with the most compressive principal strain rates ($\cos\varphi_3 \to 1$), such as $C < 0.3$ for the hydrogen flames and C close to 0 for the iso-octane flames. Differences in the alignment characteristics between the hydrogen and the iso-octane flames are consistent with the differences in the dilation rates, $\tau_\eta \Delta$, as shown in figure 4. The alignment with the most compressive principal strain rates indicates that turbulence presses the iso-surfaces together and increases the gradients of the scalar fields. This is consistent with the iso-surfaces of passive mixing scalars in turbulent flows (Kerr 1985; Ashurst *et al.* 1987; Warhaft 2000). However, for regions with high dilatation rates, the surface normals align preferentially with the most extensive principal strain rates ($\cos\varphi_1 \to 1$), such as $C = 0.7$ for the hydrogen flames and $C = 0.4$ for the iso-octane flames. This is attributed to the fact that the dilatation due to combustion strongly accelerates the flow in the flame normal direction resulting in extensive strain rates in this direction, which indicates that the dilatation pushes the iso-surfaces away from each other and decreases the scalar gradient. This competing effect of turbulence and dilatation determines the alignment of the principal strain rates in premixed flames. Similar effects of dilatation on the alignment characteristics have also been found and discussed in previous studies (Swaminathan & Grout 2006; Chakraborty & Swaminathan 2007; Kim & Pitsch 2007; Wang *et al.* 2016, 2017). For flames with sufficiently high Karlovitz numbers, where the turbulent strain rates are dominant over the flame-induced dilatation, the flame normals tend to align with the most compressive principal strain rates even in reaction zones (Hamlington, Poludnenko & Oran 2011; Wang *et al.* 2016, 2017). In addition, Wang *et al.* (2016, 2017) have demonstrated that these alignment statistics can significantly depend on the axial distance in jet flames. In the upstream region close to the nozzle exit, where the flame remains laminar-like, there is no preferential alignment between the flame normal and the most compressive or extensive principal strain rates. However, how this impacts the tangential strain rate, which is a key factor for flame–turbulence interactions and the flame surface wrinkling, is not yet fully understood because, considering the importance of the alignment characteristics for the tangential strain rate, the dependence of the alignment characteristics on the reaction progress variable and the Lewis number appear to contradict the independence of the tangential strain rate on these parameters. The same mean tangential strain rate in regions with and without dilation implies a general effect of turbulence on the tangential strain rate, which is not influenced by dilatation and the alignment of the principal strain rates.

3.3. *Decomposition of the impact of dilatation and solenoidal turbulence*

Inspired by the constant scaling of the tangential strain rate with the Kolmogorov time scale observed in figure 4 and incompressible flows (Girimaji & Pope 1990; Yeung *et al.* 1990; Gauding *et al.* 2022), it is hypothesized that small-scale turbulence governs the tangential strain rate in premixed flames in the same way as in incompressible flows, despite the presence of dilatation. To test this hypothesis, the effects of dilatation and the residual solenoidal turbulence, which features zero divergence, are examined separately. The separate treatment of solenoidal and dilatational parts of turbulent flows has been applied in various studies on compressible flows (Wang *et al.* 2018; Panickacheril John, Donzis & Sreenivasan 2021; Zheng *et al.* 2021, 2022; Sabelnikov *et al.* 2023) using the Helmholtz decomposition (Helmholtz 1858). In this study, an approach similar to

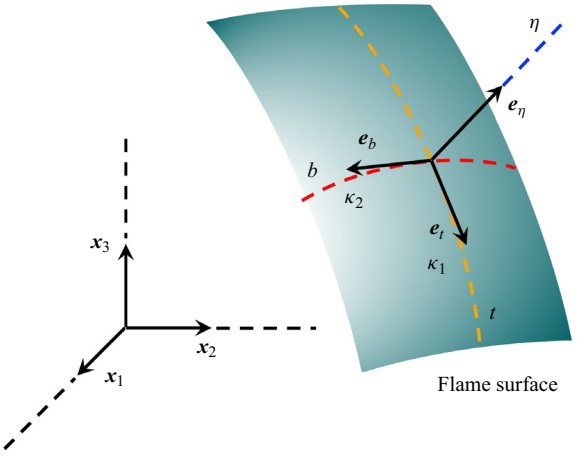

Figure 6. The flame Darboux frame.

the Helmholtz decomposition is proposed to separate the solenoidal and dilatational contributions in the velocity gradient tensor in the context of premixed flames. The main idea behind the separation approach is that the local flow caused by flame dilatation is mainly in the direction of the flame surface normal and does not change significantly in the directions tangential to the surface. For the derivation, it is convenient to introduce a local curvilinear coordinate system (η, t, b) attached to the flame surface, as also applied by Thiesset *et al.* (2017), since the effects of dilatation depend on the normal direction and the topology of the flame surface. Here, η is the distance to the surface along the normal, and b and t are the curvilinear coordinates on the flame surface aligned with the principal directions of curvature at each point of the surface as shown in figure 6. This coordinate system is also referred to as the Darboux frame in differential geometry (Prautzsch & Boehm 2018). The corresponding base vectors in the normal, tangential and binormal directions are denoted by $\boldsymbol{e}_\eta$, $\boldsymbol{e}_t$ and $\boldsymbol{e}_b$, respectively. Here, $\boldsymbol{e}_t$ and $\boldsymbol{e}_b$ are the directions of the principal curvatures κ_1 and κ_2 with $\kappa_1 > \kappa_2$. The directions are specified such that $\boldsymbol{e}_\eta$ points in the direction of the unburned gas and $\boldsymbol{e}_b = \boldsymbol{e}_t \times \boldsymbol{e}_\eta$.

The velocity gradient tensor, $\nabla \boldsymbol{u}$, is decomposed into two parts:

$$\nabla \boldsymbol{u} = \nabla \boldsymbol{u}_s + \nabla \boldsymbol{u}_d, \tag{3.6}$$

where $\nabla \boldsymbol{u}_s$ and $\nabla \boldsymbol{u}_d$ denote the contributions from solenoidal turbulence and dilatation, respectively, so that

$$\Delta = \nabla \cdot \boldsymbol{u} = \nabla \cdot \boldsymbol{u}_d \quad \text{and} \quad \nabla \cdot \boldsymbol{u}_s = 0. \tag{3.7a,b}$$

In the following, $\nabla \boldsymbol{u}_d$ in the flame Darboux frame is derived. The flame Darboux frame simplifies the derivation since $\nabla \boldsymbol{u}_d$ depends on the normal direction and the topology of the flame surface. Assume that the local flow caused by flame dilatation is only in the direction of the normal vector and does not change strongly in the directions tangential to the surface:

$$\left.\begin{aligned} u_{d,t} = u_{d,b} = 0, \\ \frac{\partial u_{d,\eta}}{\partial t} = \frac{\partial u_{d,\eta}}{\partial b} = 0, \end{aligned}\right\} \tag{3.8}$$

where $u_{d,t}$, $u_{d,b}$ and $u_{d,\eta}$ are the components of $\boldsymbol{u}_d$ in the direction of $\boldsymbol{e}_t$, $\boldsymbol{e}_b$ and $\boldsymbol{e}_\eta$, respectively. It is worth noting that such assumptions may be invalid in flame surface

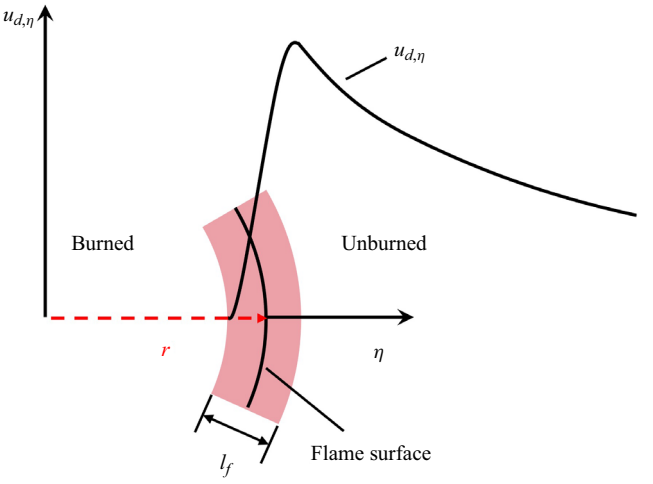

Figure 7. Schematic of local dilatation-induced velocity.

regions with high curvatures. However, as will be shown in figure 9, for the investigated flames in the thin reaction zones regime, the main fraction of the flame surface ($\geq$85 %) exhibits small curvatures compared with the reciprocal of the flame thickness. The velocity gradient $\boldsymbol{\nabla u}_d$ is then simplified as

$$\boldsymbol{\nabla u}_d = \frac{\partial u_{d,\eta}}{\partial \eta}\boldsymbol{e}_\eta\boldsymbol{e}_\eta + \kappa_1 u_{d,\eta}\boldsymbol{e}_t\boldsymbol{e}_t + \kappa_2 u_{d,\eta}\boldsymbol{e}_b\boldsymbol{e}_b, \tag{3.9}$$

where only components on the diagonal are present. For a given flame surface, $\boldsymbol{e}_\eta$, $\boldsymbol{e}_t$, $\boldsymbol{e}_b$, κ_1 and κ_2 in (3.9) are known; however, $\partial u_{d,\eta}/\partial\eta$ and $u_{d,\eta}$ are unknown and determined by the following procedure. The dilatation rate is known and given by

$$\Delta = \boldsymbol{\nabla}\cdot\boldsymbol{u}_d = \frac{\partial u_{d,\eta}}{\partial \eta} + \kappa_1 u_{d,\eta} + \kappa_2 u_{d,\eta}. \tag{3.10}$$

There is only one equation (3.10) available for two unknown variables $\partial u_{d,\eta}/\partial\eta$ and $u_{d,\eta}$, so another relation is needed. Figure 7 illustrates schematically the local dilatation-induced velocity, where $r = 1/\kappa$ is the radius of curvature κ. For small curvature with $r \gg l_f$, $\kappa u_{d,\eta} = u_{d,\eta}/r$ is negligible compared with $\partial u_{d,\eta}/\partial\eta$. For large curvature, it applies $\kappa u_{d,\eta} = u_{d,\eta}/r \approx \partial u_{d,\eta}/\partial\eta$. Therefore, a relation between $\partial u_{d,\eta}/\partial\eta$ and $\kappa_1 u_{d,\eta}$ or $\kappa_2 u_{d,\eta}$ can be determined based on the flame thickness, l_f, and the principal curvature with the larger magnitude, κ_m. It is assumed that

$$\begin{cases} \kappa_1 u_{d,\eta} = \kappa_2 u_{d,\eta} = 0 & \text{if } |\kappa_m| < 1/l_f \\ \kappa_m u_{d,\eta} = \dfrac{\partial u_{d,\eta}}{\partial \eta},\ \kappa_n u_{d,\eta} = \dfrac{\kappa_n}{\kappa_m}\dfrac{\partial u_{d,\eta}}{\partial \eta} & \text{otherwise,} \end{cases} \tag{3.11}$$

where

$$\begin{cases} m = 1, n = 2 & \text{if } |\kappa_1| > |\kappa_2| \\ m = 2, n = 1 & \text{otherwise.} \end{cases} \tag{3.12}$$

Here, κ_1 and κ_2 can be positive or negative. Additionally, l_f is influenced by flame interactions with turbulence and thermodiffusive instabilities, and thus can be different

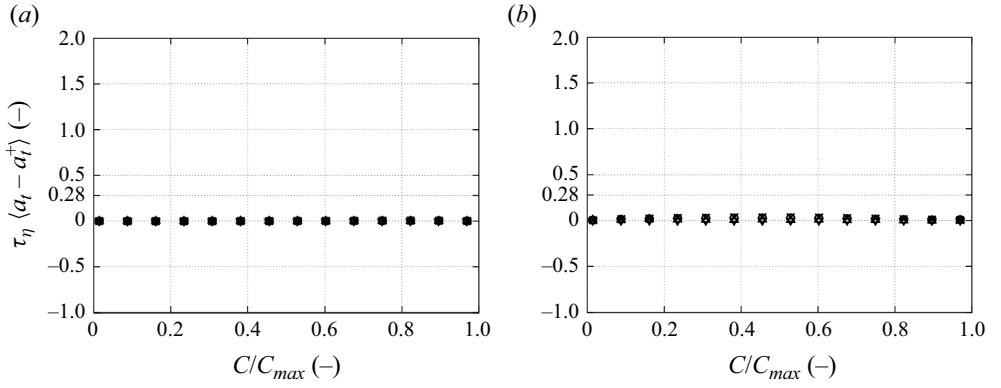

Figure 8. Effects of dilatation on the normalized tangential strain rate $\tau_\eta a_t$. The superscript + denotes a quantity evaluated using $\nabla \boldsymbol{u}_s$ in (3.6). Symbols represent the conditional surface average for different cases as given in figure 4. (*a*) Hydrogen and (*b*) iso-octane. For the sake of comparability, the range of the *y*-axis is kept the same as the tangential strain rate in figure 4.

from the thickness of the corresponding unstretched laminar flames. In this study, l_f for the turbulent flames is computed from the maximum conditional mean of the reaction progress variable gradient conditioned on the reaction progress variable, $\max\{\overline{\nabla C}_C\}$, where C is the reaction progress variable. According to (3.9), (3.10), (3.11) and (3.12), $\nabla \boldsymbol{u}_d$ in the global coordinate system can be expressed as in (3.13). The effects of solenoidal turbulence on the tangential strain rate can be evaluated by only considering the contributions of $\nabla \boldsymbol{u}_s$, which can be obtained by (3.6) and (3.13).

$$\nabla u_{d,ij} = \begin{cases} \Delta \boldsymbol{e}_{\eta,i}\boldsymbol{e}_{\eta,j} & \text{if } |\kappa_1|, |\kappa_2| < \dfrac{1}{l_f}, \\ \dfrac{\Delta}{2+\kappa_2/\kappa_1}\boldsymbol{e}_{\eta,i}\boldsymbol{e}_{\eta,j} + \dfrac{\Delta}{2+\kappa_2/\kappa_1}\boldsymbol{e}_{t,i}\boldsymbol{e}_{t,j} + \dfrac{\Delta\kappa_2/\kappa_1}{2+\kappa_2/\kappa_1}\boldsymbol{e}_{b,i}\boldsymbol{e}_{b,j} & \text{if } |\kappa_1| > \dfrac{1}{l_f} \\ & \quad \text{and } |\kappa_1| > |\kappa_2|, \\ \dfrac{\Delta}{2+\kappa_1/\kappa_2}\boldsymbol{e}_{\eta,i}\boldsymbol{e}_{\eta,j} + \dfrac{\Delta\kappa_1/\kappa_2}{2+\kappa_1/\kappa_2}\boldsymbol{e}_{t,i}\boldsymbol{e}_{t,j} + \dfrac{\Delta}{2+\kappa_1/\kappa_2}\boldsymbol{e}_{b,i}\boldsymbol{e}_{b,j} & \text{if } |\kappa_2| > \dfrac{1}{l_f} \\ & \quad \text{and } |\kappa_2| > |\kappa_1|. \end{cases} \tag{3.13}$$

Contributions of dilatation on the tangential strain rate expressed as $\langle a_t - a_t^+ \rangle$ are shown in figure 8. Quantities evaluated with $\nabla \boldsymbol{u}_s$ are denoted by the superscript '+'. For most of the flame regions, the tangential strain rate is not influenced significantly by dilatation, which is illustrated by the almost zero value of $\langle a_t - a_t^+ \rangle$. This is consistent with figure 4 and demonstrates that for most of the flame surface, dilation only influences the velocity gradient in the direction of the flame normal. According to (3.13), this corresponds to the surface segments with $|\kappa_1|, |\kappa_2| < 1/l_f$. As shown in figure 9, most of the flame surface (>80 %) is under this condition. Note that for highly curved flame segments, dilatation affects also the velocity gradient tangential to the flame surface.

3.4. *Alignment of the flame normal with the principal strain rates evaluated using* $\nabla \boldsymbol{u}_s$

In this section, the alignment characteristics of the principal strain rates of the solenoidal turbulence evaluated with the decomposed velocity gradient, $\nabla \boldsymbol{u}_s$ in (3.6), are analysed. As shown in figure 10, surface normals align preferentially with the most compressive

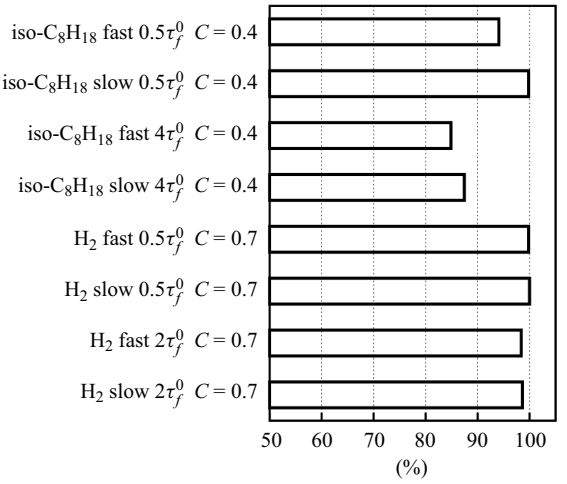

Figure 9. Percentage of surface with $|\kappa_1|, |\kappa_2| < 1/l_f$.

principal strain rates across the entire flame for all eight cases, which is almost independent of C and consistent with the alignment characteristics for material surfaces in incompressible flows. This indicates that even in regions with high dilatation, the residual solenoidal turbulence has the same effect as in regions without dilatation. It orients the flame surface such that the surface normals align with the most compressive principal strain rates of the solenoidal turbulence. It is remarkable that even though the flame interactions with turbulence and thus the flame kernel topology are significantly different between the hydrogen and iso-octane flame kernels and different realizations of each fuel (cf. figure 3), the local flame surface direction is always determined by the solenoidal turbulence independent of the Lewis number and the location of the surface in the flame. In addition, even at $0.5\tau_f^0$, which is shortly after ignition with substantial ignition effects and not much flame surface wrinkling has been developed, especially for the slow kernels, the same behaviour is obtained. This is consistent with Girimaji & Pope (1992), who showed that the preferential alignment of initially randomly oriented surface elements with the principal strain rates is obtained after an initial transient period of a few Kolmogorov time scales, which indicates that the surface reorientation is a small-scale phenomenon. The fact that the general behaviour also applies to the very early phase in the flame kernel development is of vital importance for the modelling of flame kernels since the kernel growth rates correlate significantly to the tangential strain rate at $0.5\tau_f^0$ in the investigated DNS (Chu *et al.* 2023*a*). An illustration of the directions of the local instantaneous principal strain rates evaluated using $\nabla \boldsymbol{u}$ and $\nabla \boldsymbol{u}_s$ is given in figure 11. The dilatation changes the directions of the principal strain rates. The surface normal aligns with the most extensive principal strain rate, e_1, evaluated using $\nabla \boldsymbol{u}$, while it aligns with the most compressive principal strain rate, e_3^+, evaluated using $\nabla \boldsymbol{u}_s$. It can be concluded that the tangential strain rate is mainly determined by the strain rates of the solenoidal turbulence and their orientation with respect to the flame surface, similarly to material surfaces in incompressible flows. The apparent contradiction between (i) the independence of the normalized tangential strain rate on dilation and (ii) the strong dependence of the alignment characteristics of the principal strain rates evaluated with $\nabla \boldsymbol{u}$ on dilatation is because dilatation due to combustion does not contribute significantly to the tangential

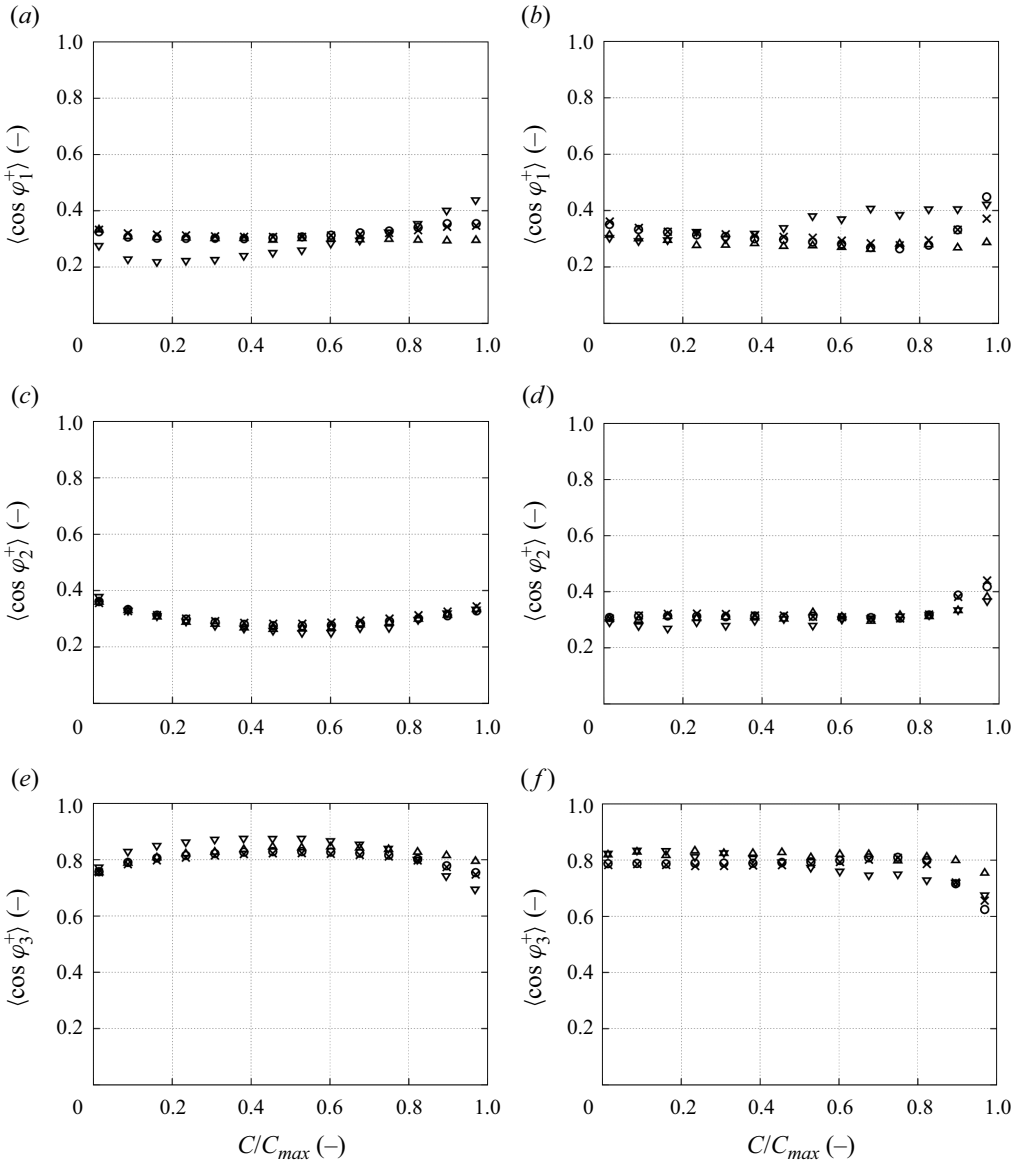

Figure 10. Alignment characteristics between the principal strain rates and the iso-surfaces of C, expressed by $\cos \varphi_i^+$, as a function of C. The superscript + denotes a quantity evaluated using $\nabla \boldsymbol{u}_s$ in (3.6). Symbols represent the conditional surface average for different cases as given in figure 4. (*a*,*c*,*e*) Hydrogen and (*b*,*d*,*f*) iso-octane.

strain rate, but influences significantly the strain rate tensor and thus the alignment of the principal strain rates of the undecomposed velocity field.

It is worth noting that the effects of the amount of energy deposition on the alignment of the flame surface normals with the principal strain rates and the tangential strain rates need further investigation. In particular, for large energy deposition, the flame propagation can be significantly accelerated by the ignition, which might change the flame interactions with turbulence. As will be discussed in § 3.6, if the flame propagation speed is sufficiently large compared to the Kolmogorov velocity, no preferential alignment of the flame normal

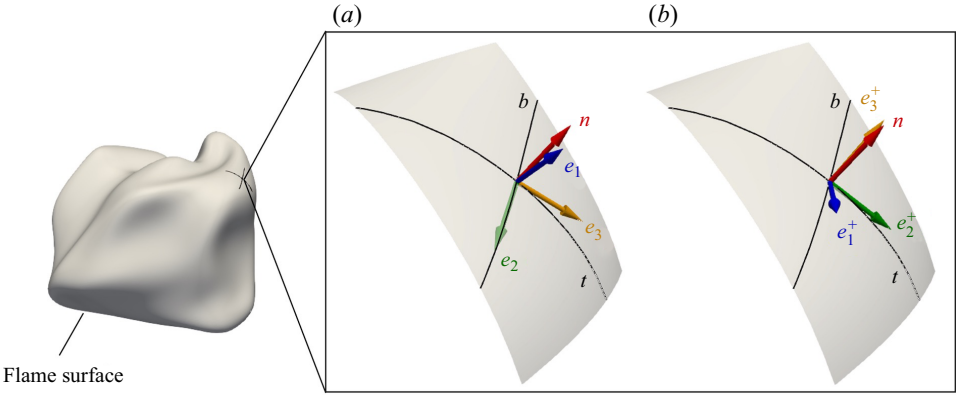

Figure 11. Illustration of the directions of the principal strain rates. (*a*) e_i, evaluated using $\nabla \boldsymbol{u}$, and (*b*) e_i^+, evaluated using $\nabla \boldsymbol{u}_s$ in (3.6).

with the principal strain rates can be obtained, which will result in lower tangential strain rates.

3.5. *Correlations between local tangential strain rate and small-scale turbulence*

3.5.1. *Tangential strain rate and small-scale turbulence evaluated using* $\nabla \boldsymbol{u}$

The initial flame kernels are relatively small compared to the turbulent integral length scale. As a result, their tangential strain rate is predominantly influenced by the local instantaneous small-scale turbulence and may not be adequately represented by the ensemble-averaged quantities of the HIT. Therefore, it is of relevance to evaluate the impact of local small-scale turbulence on the local tangential strain rate. Typically, the local small-scale turbulence is quantified by the velocity gradient tensor, its symmetric (the strain rate tensor) or skew-symmetric (the rotation tensor) parts, or their invariants (Soria *et al.* 1994; Blackburn, Mansour & Cantwell 1996; Elsinga & Marusic 2010; Breda & Buxton 2019). However, in this study, inspired by the scaling of the tangential strain rate with the Kolmogorov time scale, the small-scale turbulence is expressed as $(\nu/\epsilon)^{1/2}$, where ν and ϵ are the local instantaneous viscosity and turbulence dissipation rate, respectively. This definition corresponds to a local small-scale time, which is different from the Kolmogorov time $\tau_\eta = (\nu/\bar{\epsilon})^{1/2}$ used for the normalization in figure 4 with the average dissipation rate $\bar{\epsilon}$. Figure 12 shows the tangential strain rate as a function of the reciprocal of such local small-scale time. Both quantities are normalized with the Kolmogorov time evaluated in the unburned mixture τ_η. Statistics are taken for two iso-surfaces of C for each fuel, which correspond to C with the maximum dilatation rate ($C = 0.4$ for iso-octane and $C = 0.7$ for hydrogen cf. figure 4) and negligible dilatation rate ($C = 0.02$). For $C = 0.02$, the correlations between the local tangential strain rate and the small-scale turbulence are almost the same for both fuels. An almost linear positive correlation can be identified for all the cases of each fuel, which agrees well with the slope of 0.28. However, distinctly different behaviours of different cases are observed in regions with high dilatation rates. In particular, a negative correlation is observed for the slow iso-octane kernel at $0.5\tau_f^0$. Figures 13 and 14 show the alignment characteristics as a function of $\tau_\eta/(\nu/\epsilon)^{1/2}$ for $C = 0.02$ (negligible dilatation rate) and in the regions with high dilatation, respectively. For $C = 0.02$, a similar behaviour is observed for both fuels. The flame normals preferentially align with the most compressive principal strain rate

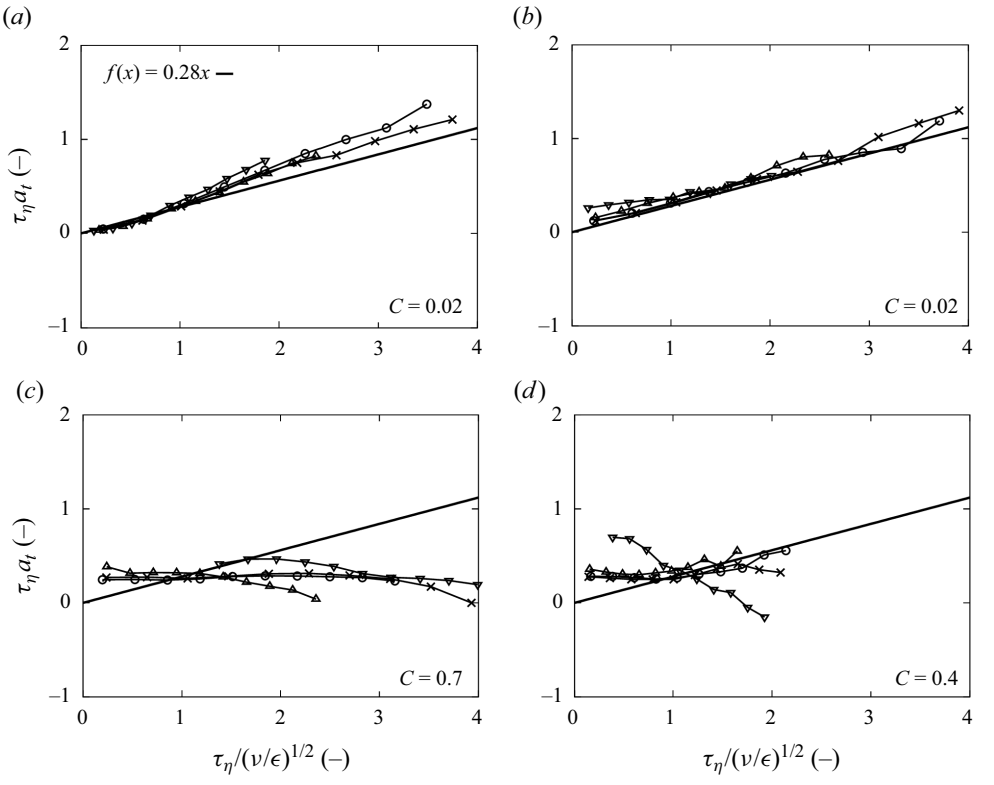

Figure 12. Normalized tangential strain rate $\tau_\eta a_t$ as a function of small-scale turbulence, expressed by $\tau_\eta/(\nu/\epsilon)^{1/2}$. Both variables are normalized with the Kolmogorov time evaluated in the unburned mixture, τ_η. Symbols represent the conditional surface average for different cases as given in figure 4. (*a*,*c*) Hydrogen and (*b*,*d*) iso-octane.

and this preferential alignment tends to increase with increasing $\tau_\eta/(\nu/\epsilon)^{1/2}$ for all the cases. This is expected, since a stronger velocity gradient means a higher likelihood of the surface normal being oriented by the flow, which results in a preferential alignment of the surface normals with the most compressive principal strain rates. However, in regions with large dilatation (figure 14), different behaviours are observed for different cases. In particular, for hydrogen flame kernels and the slow iso-octane kernel at $0.5\tau_f^0$, which exhibit high dilatation, $\tau_\eta \Delta$ (figure 4), the flame normals preferentially align with the most extensive principal strain rates and this preferential alignment tends to increase with increasing $\tau_\eta/(\nu/\epsilon)^{1/2}$. Such different correlations in the presence of dilatation imply that the quantity describing the small-scale turbulence, which contains both the effects of the solenoidal turbulence and dilatation, is 'polluted' by the dilatation. It is hypothesized that only the solenoidal component, rather than the entire small-scale flow, is the decisive parameter and a more general behaviour is expected when only considering the solenoidal turbulence, which is consistent with the material surfaces in incompressible flows. This hypothesis and the 'pollution' of the dilatation in the small-scale turbulence are assessed in the next section.

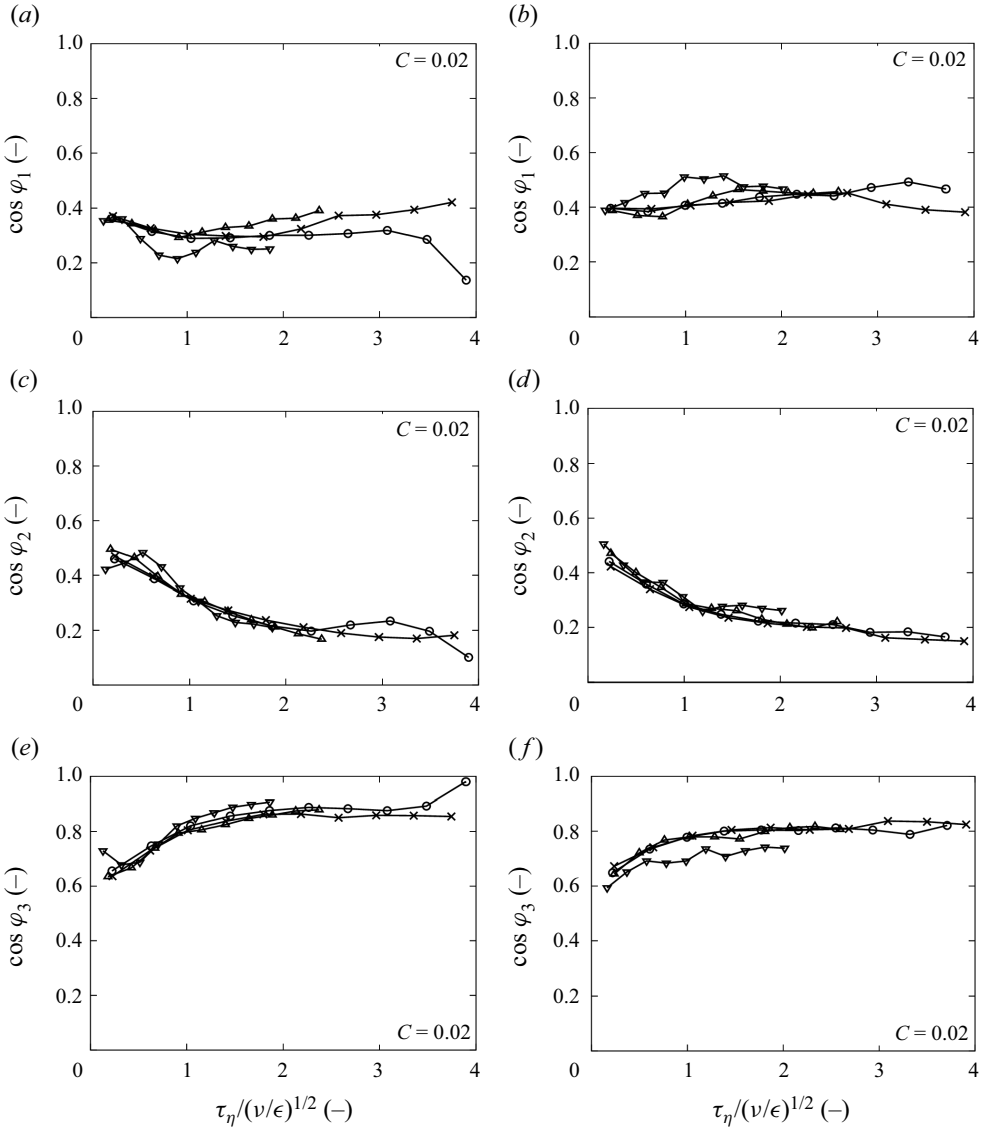

Figure 13. Alignment characteristics between the principal strain rates and the iso-surfaces of C, expressed by $\cos\varphi_i$, as a function of $\tau_\eta/(\nu/\epsilon)^{1/2}$ for $C = 0.02$ (negligible dilatation rate). Symbols represent the conditional surface average for different cases as given in figure 4. (*a*,*c*,*e*) Hydrogen and (*b*,*d*,*f*) iso-octane.

3.5.2. *Tangential strain rate and small-scale turbulence evaluated using* $\nabla \boldsymbol{u}_s$

In this section, quantities evaluated using the solenoidal turbulence, $\nabla \boldsymbol{u}_s$, in the regions with high dilatation rate are assessed. As demonstrated in figure 15, the effects of small-scale solenoidal turbulence on the local tangential strain rate in the regions with high dilatation are almost identical for both fuels and very similar to the characteristics obtained from the iso-surface of $C = 0.02$ in figure 12 with a slope close to 0.28. The dependence of the alignment characteristics is shown in figure 16. The same behaviour is observed for different cases and is similar to the region with low dilatation in figure 13. This is remarkable since the flame response to turbulence of the two fuels is distinctly

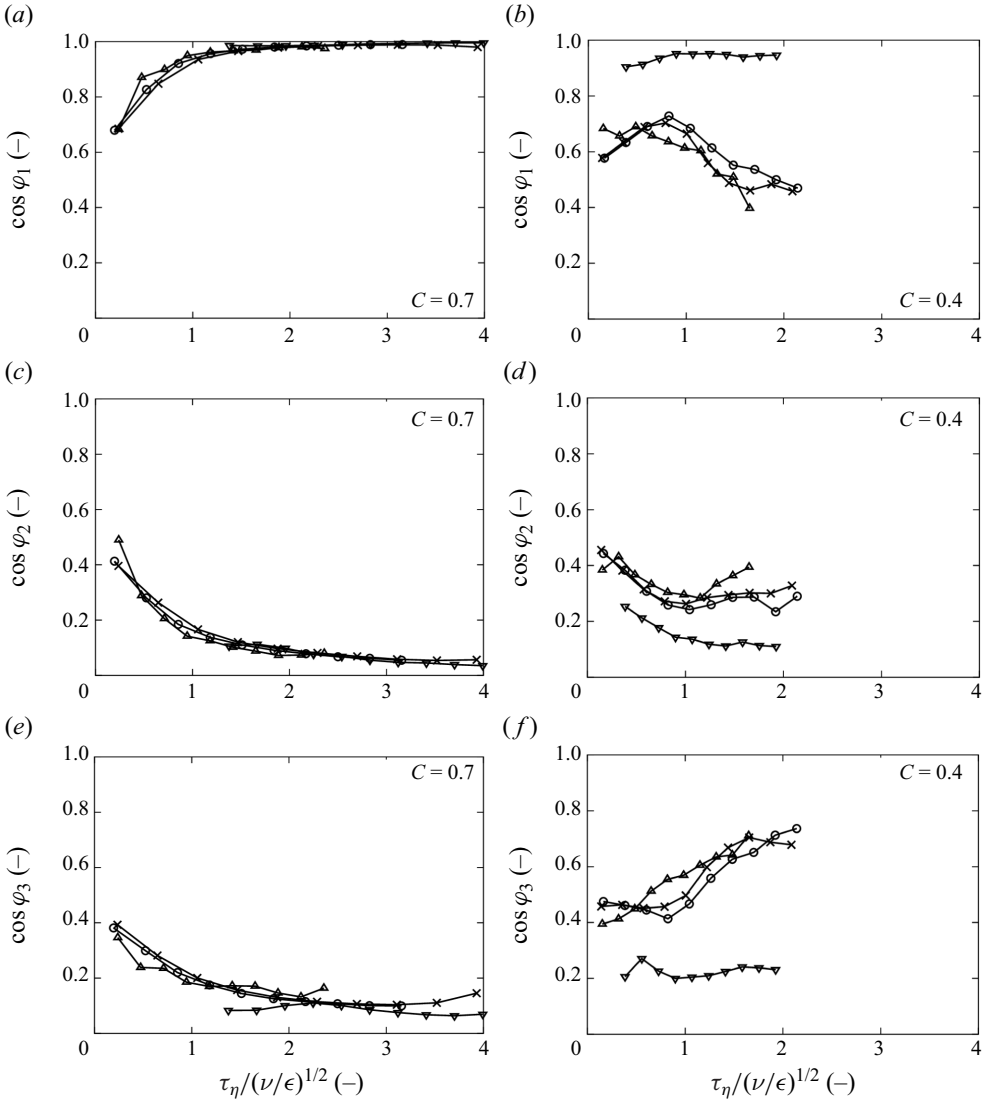

Figure 14. Alignment characteristics between the principal strain rates and the iso-surfaces of C, expressed by $\cos\varphi_i$, as a function of $\tau_\eta/(\nu/\epsilon)^{1/2}$ for regions with high dilatation rate. Symbols represent the conditional surface average for different cases as given in figure 4. (*a*,*c*,*e*) Hydrogen and (*b*,*d*,*f*) iso-octane.

different due to the significantly different Lewis numbers (cf. table 1). In particular, the hydrogen flames feature strong thermodiffusive instabilities resulting in a very different flame topology compared with the iso-octane flames as shown in figure 3. Such general behaviour indicates that the effects of the solenoidal turbulence on the flame surface straining and the orientation of the surface are not influenced by the Lewis numbers. This general behaviour also validates the assumptions of (3.8) for the investigated flames.

Dilatation changes not only the direction of the principal strain rates but also the local dissipation rate and thus the normalized local small-scale time $\tau_\eta/(\nu/\epsilon)^{1/2}$. Figure 17 shows the difference between the normalized local small-scale time $\tau_\eta/(\nu/\epsilon)^{1/2}$ evaluated using the undecomposed velocity field and $\tau_\eta/(\nu/\epsilon^+)^{1/2}$ evaluated using the

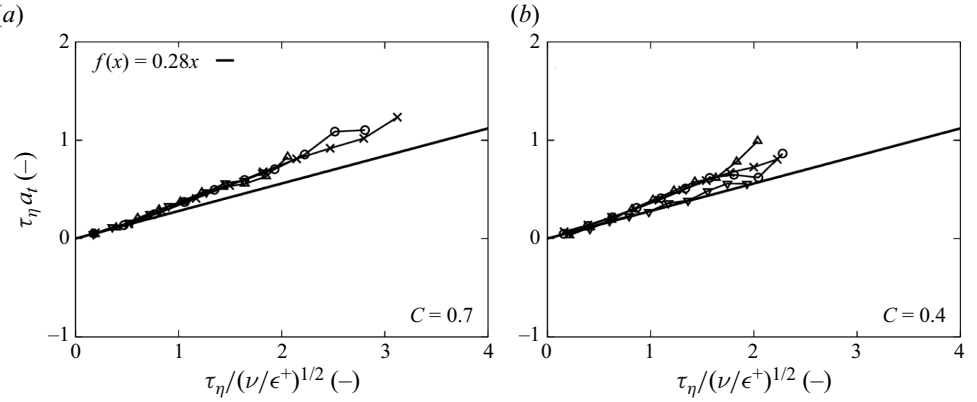

Figure 15. Normalized tangential strain rate $\tau_\eta a_t$ as a function of small-scale turbulence, expressed by $\tau_\eta/(\nu/\epsilon^+)^{1/2}$. The superscript + denotes a quantity evaluated using $\nabla \boldsymbol{u}_s$ in (3.6). Both variables are normalized with the Kolmogorov time evaluated in the unburned mixture, τ_η. Symbols represent the conditional surface average for different cases as given in figure 4. (*a*) Hydrogen and (*b*) iso-octane.

solenoidal turbulence. In regions with high dilatation, $\tau_\eta/(\nu/\epsilon)^{1/2}$ is increased. In other regions, $\tau_\eta/(\nu/\epsilon)^{1/2}$ can also be reduced by dilatation. Due to such effects of dilatation on the local velocity gradient as well as the dissipation rate, the correlation between the tangential strain rate or the alignment characteristics and $\tau_\eta/(\nu/\epsilon)^{1/2}$ is ambiguous in regions with high dilatation (figures 12 and 14).

3.6. *Consideration of the universality of the behaviour of* $\tau_\eta\langle a_t\rangle_s$

With the decomposition, it has been shown that the tangential strain rate at the surfaces in premixed flames is mainly determined by the solenoidal part of the turbulence through the same mechanism as the material surfaces in incompressible flows: surfaces are oriented by the velocity gradients, which results in preferential alignments of the surface normal with the most compressive strain rate and yields a value of the normalized tangential strain rate of $\tau_\eta\langle a_t\rangle_s \approx 0.28$ (Yeung *et al.* 1990; Girimaji & Pope 1992). It is of practical importance to understand under which conditions this holds valid in premixed flames. The preferential alignment can be observed only if the strain rates have enough time to interact with the surface elements. For surfaces with propagating velocities much larger than the Kolmogorov velocity scale, v_η, which propagate through different turbulent eddies with different orientations very rapidly, the strain rates experienced by the surfaces are too fleeting to orient the surfaces. Girimaji & Pope (1992) investigated the straining of propagating surfaces in HIT and found that the tangential strain rate decreases with increasing propagation speed. Gauding *et al.* (2022) also reported a substantial decrease in the tangential strain rate of iso-surfaces of mixing scalars when the scalar diffusivity is increased. For premixed flames, the propagating velocity of the flame surface relative to the Kolmogorov velocity scale can be characterized by the Karlovitz number,

$$Ka = \frac{\tau_f^0}{\tau_\eta} \approx \frac{(l_f^0)^2}{\eta^2}. \tag{3.14}$$

The ratio of the flame speed to the Kolmogorov velocity scale is given as

$$\frac{s_l^0}{v_\eta} = \frac{l_f^0/\tau_f^0}{l_\eta/\tau_\eta} \approx \frac{1}{\sqrt{Ka}}. \tag{3.15}$$

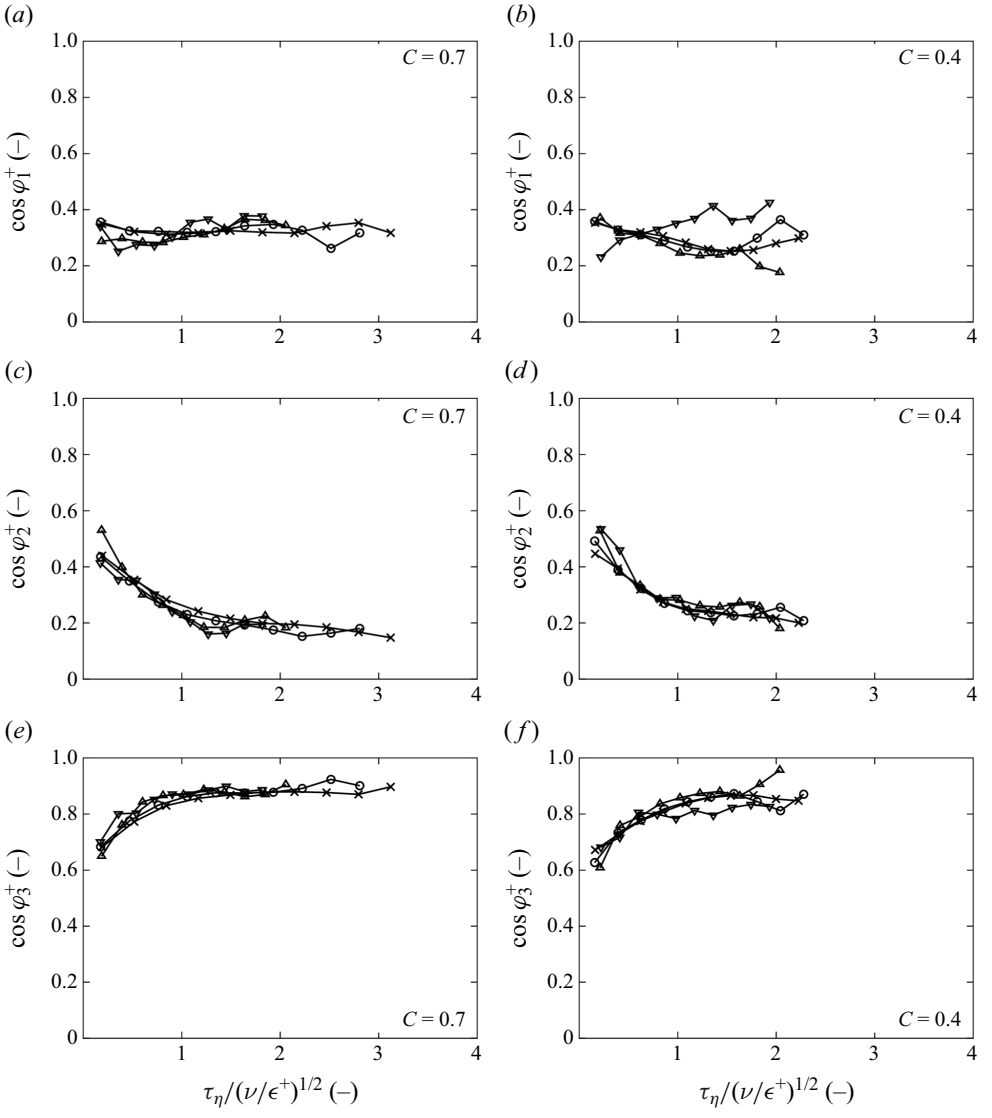

Figure 16. Alignment characteristics between the principal strain rates and the iso-surfaces of C, expressed by $\cos\varphi_i^+$, as a function of $\tau_\eta/(\nu/\epsilon^+)^{1/2}$. The superscript + denotes a quantity evaluated using $\nabla \boldsymbol{u}_s$ in (3.6). Symbols represent the conditional surface average for different cases as given in figure 4. (*a*,*c*,*e*) Hydrogen and (*b*,*d*,*f*) iso-octane.

Therefore, for flames in the thin reaction zones regimes ($Ka > 1$), where the propagation speed of the flame surface is small compared to the Kolmogorov velocity scale and the flame surface can be approximated as a material surface, the value of $\tau_\eta\langle a_t\rangle_s \approx 0.28$ is expected. For flames in the corrugated flamelet regime ($Ka < 1$), the smallest eddy has less time to orient the surface and thus a lower value of the normalized tangential strain can be expected, which is supported by the results of Dopazo *et al.* (2015), who reported a normalized mean tangential strain rate of approximately 0.08 for a flame with $Ka = 0.68$. For flames in the broken reaction zones regime, even though the Karlovitz number is also larger than unity, the behaviour of the tangential strain rate might be different from

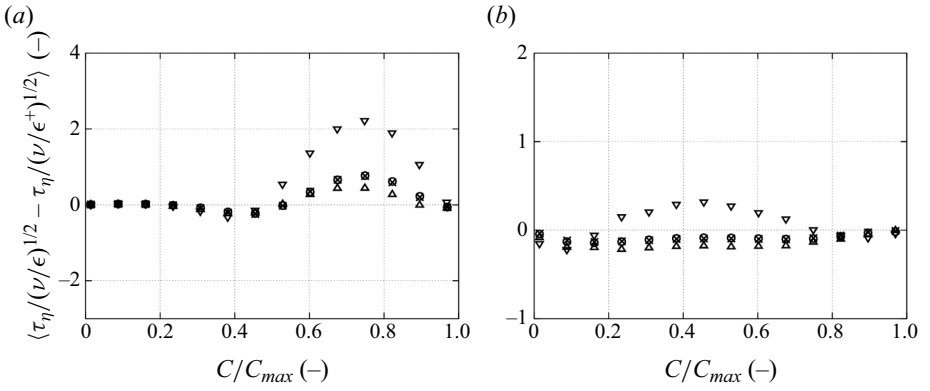

Figure 17. Effects of dilatation on the small-scale turbulence expressed by $\tau_\eta/(\nu/\epsilon)^{1/2}$. The superscript + denotes a quantity evaluated using $\nabla \boldsymbol{u}_s$ in (3.6). Symbols represent the conditional surface average for different cases as given in figure 4. (*a*) Hydrogen and (*b*) iso-octane.

the straining of material surfaces in incompressible flows since the flame regions of high curvature will increase, where the dilatation not only acts in the flame normal direction but also in the tangential directions according to (3.13), and the assumptions of (3.8) may be invalid. In addition, Krisman *et al.* (2021) have shown that for extinguishing flame kernels with $Ka > 100$, significant flame–flame interactions exist, which might also change the behaviour of the tangential strain rate for flames in the broken reaction zones regime. It is worth noting that the tangential strain rate can also be influenced by the configuration. Wang *et al.* (2016, 2017) investigated the tangential strain rates of a premixed jet flame. They have shown that the tangential strain rate in the region close to the nozzle exit is smaller than in downstream regions due to the unsteadiness of turbulence near the nozzle exit.

4. Conclusions

The tangential strain rate and the alignment characteristics between the principal strain rates and the flame surface are investigated using direct numerical simulations of premixed hydrogen and iso-octane flames in the thin reaction zones regime under engine conditions. The investigated flames feature significantly different Lewis numbers and thus flame–turbulence interactions.

Tangential strain rates in all investigated flames show a similar average value of approximately 0.28 when normalized with the Kolmogorov time scale. This value is not influenced by the alignment of the flame surface normal with the principal strain rates, which have been identified as the reason for the same value of the normalized tangential strain rate of 0.28 at material surfaces in incompressible flows (Yeung *et al.* 1990). To investigate such a counter-intuitive behaviour in premixed flames, a decomposition approach is proposed to separate the effects of dilatation and residual solenoidal turbulence. It is found that such a behaviour is because dilatation due to combustion does not contribute significantly to the tangential strain rate but influences significantly the strain rate tensor and thus the orientation of the principal strain rates.

With the decomposition of the two effects, it has been shown that the tangential strain rate at the surfaces in premixed flames is mainly determined by the solenoidal part of the turbulence through the same mechanism as the material surfaces in incompressible flows: the surfaces are oriented by the velocity gradients, which results in preferential

alignments of the surface normal with the most compressive strain rate and yields a value of the normalized tangential strain rate of approximately 0.28. In addition, an almost linear correlation with a slope of 0.28 between the local tangential strain rate and the local small-scale time evaluated using the solenoidal turbulence is identified.

This general behaviour is independent of the Lewis number and the reaction progress variable and is expected to hold valid for flames in the thin reaction zones regime. These are remarkable findings indicating that models of the tangential strain rate developed based on incompressible flows (Cant *et al.* 1991; Duclos *et al.* 1993; Hawkes & Cant 2001) apply also to premixed flames with different Lewis numbers. However, for the modelling, only the solenoidal turbulence or the flow parameters conditioned on the unburned mixtures should be taken into account. In current models (Chakraborty 2021), the Favre-averaged quantities are commonly used instead of the quantities conditioned on the unburned mixtures.

Acknowledgements. The authors gratefully acknowledge the Gauss Centre for Supercomputing e.V. (www.gauss-centre.eu) for funding this project by providing computing time on the GCS Supercomputer Super-MUC at Leibniz Supercomputing Centre (LRZ, www.lrz.de).

Funding. H.P. and H.C. received funding from the Deutsche Forschungsgemeinschaft (DFG, German Research Foundation) under Research Unit FOR2687 for this research. H.P. and M.G. received funding from the European Union (ERC Advanced Grant HYDROGENATE, 101054894) for this research.

Declaration of interests. The authors report no conflict of interest.

Author ORCIDs.
Hongchao Chu https://orcid.org/0000-0001-5453-8007;
Lukas Berger https://orcid.org/0000-0001-9169-2986;
Michael Gauding https://orcid.org/0000-0003-0038-5249;
Antonio Attili https://orcid.org/0000-0003-2771-8832;
Heinz Pitsch https://orcid.org/0000-0001-5656-0961.

Appendix A

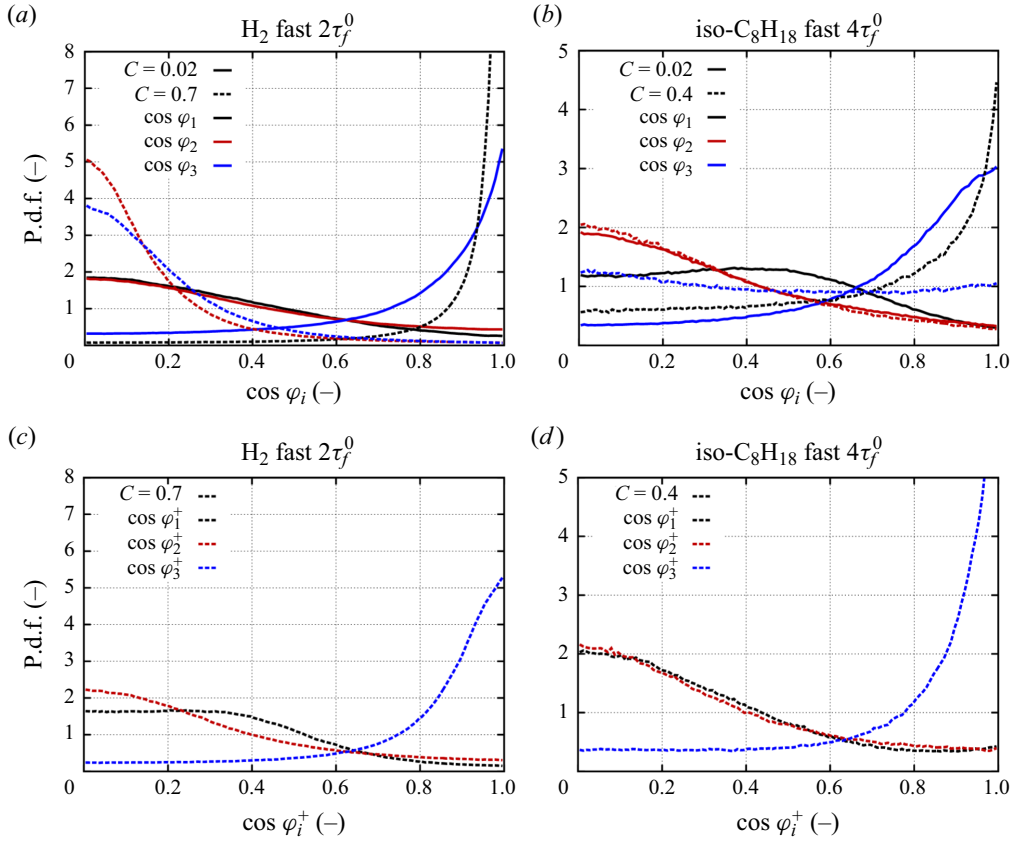

Figure 18. P.d.f. of the cosine of the angle between the direction of the principal strain rates and flame surface normal. The superscript + denotes a quantity evaluated using $\nabla \boldsymbol{u}_s$ in (3.6). (*a*,*c*) Hydrogen and (*b*,*d*) iso-octane.

Appendix B

This section presents the results of a fully developed turbulent planar iso-octane flame and the iso-octane flame kernels evaluated using the progress variable defined as $C = Y_{CO_2}$. The tangential strain rates, the dilatation rates, and the alignment characteristics of the flame normals with the principal strain rates evaluated using the undecomposed velocity field and solenoidal turbulence are shown in figures 19–29. These figures demonstrate that the primary findings discussed in the main manuscript remain unchanged for the planar turbulent flame and the iso-octane flame kernels when using a different definition of C. The DNS of the planar flame was performed for the same thermodynamic and flow conditions as the iso-octane flame kernels in this study, with an effective Lewis number of $Le_{eff} = 2.0$. The planar flame has been introduced into the simulation domain by mapping a one-dimensional laminar unstretched flame solution onto the DNS grid. A detailed description of the planar flame DNS can be found from Falkenstein *et al.* (2020*a*,*b*). The data considered in this study are at $\tau = 2.8\tau_t$ when the planar flame is fully developed in the turbulent flow.

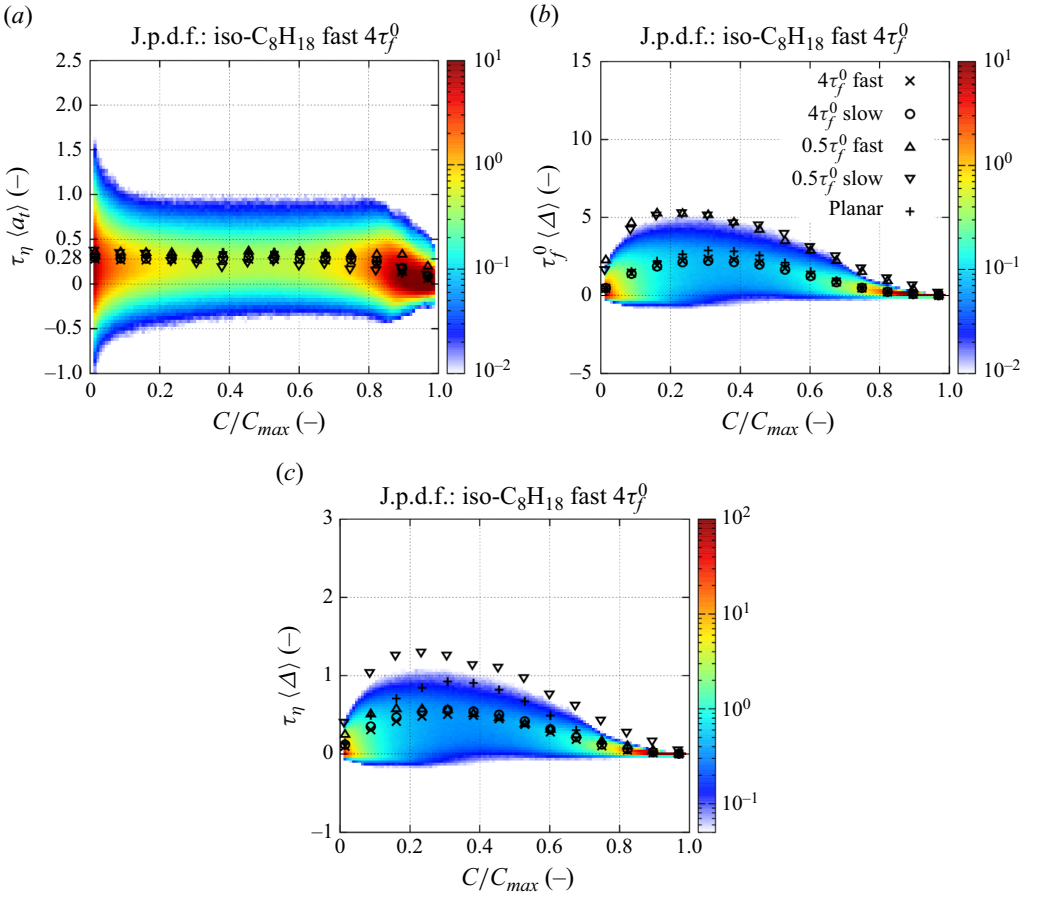

Figure 19. Normalized tangential strain rate $\tau_\eta\langle a_t\rangle$, and dilatation rate $\tau_f^0\langle\Delta\rangle$ and $\tau_\eta\langle\Delta\rangle$ as functions of C. The variables are normalized with the chemical time τ_f^0 or the Kolmogorov time τ_η, evaluated in the unburned mixture. The colour maps represent the j.p.d.f. of the fast iso-octane kernel at $4\tau_f^0$. In this figure, the progress variable is defined as $C = Y_{CO_2}$.

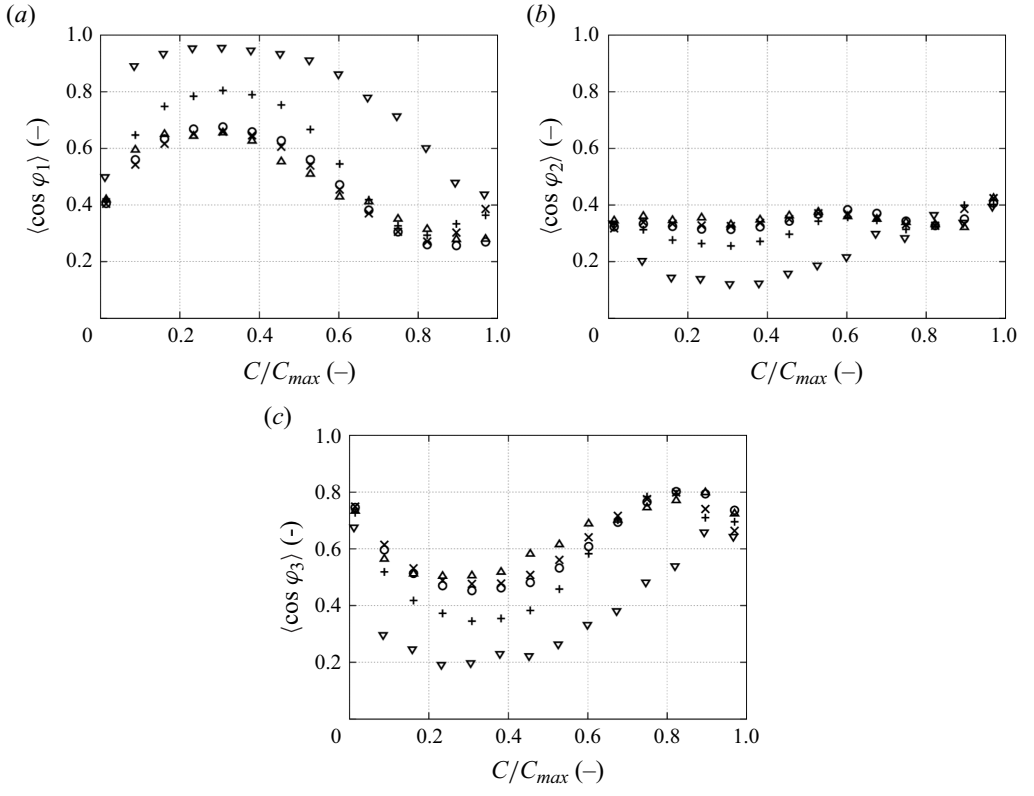

Figure 20. Alignment characteristics between the principal strain rates and the iso-surfaces of C, expressed by $\cos\varphi_i$, as a function of C. Symbols represent the conditional surface average for different cases as given in figure 19. In this figure, the progress variable is defined as $C = Y_{CO_2}$.

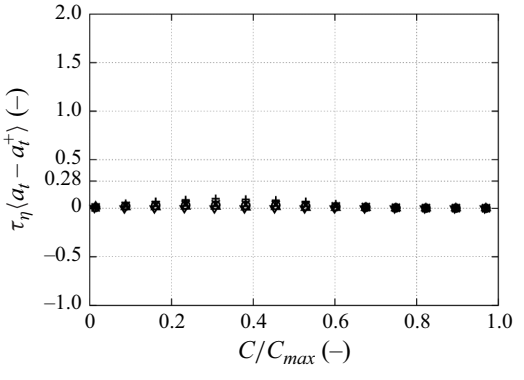

Figure 21. Effects of dilatation on the normalized tangential strain rate $\tau_\eta a_t$. The superscript $+$ denotes a quantity evaluated using $\nabla \boldsymbol{u}_s$ in (3.6). Symbols represent the conditional surface average for different cases as given in figure 19. For the sake of comparability, the range of the y-axis is kept the same as the tangential strain rate in figure 19. In this figure, the progress variable is defined as $C = Y_{CO_2}$.

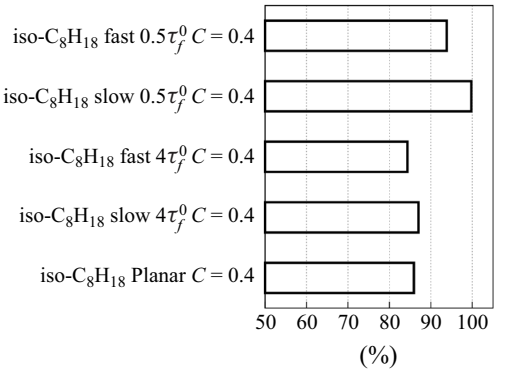

Figure 22. Percentage of surface with $|\kappa_1|, |\kappa_2| < 1/l_f$. In this figure, the progress variable is defined as $C = Y_{CO_2}$.

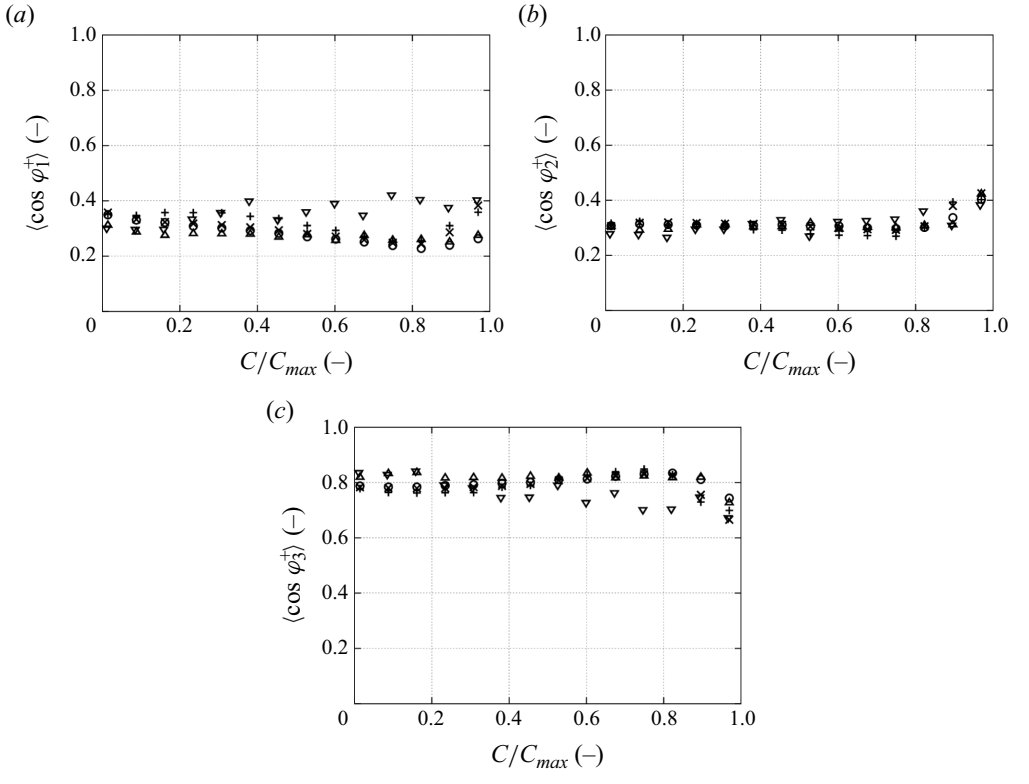

Figure 23. Alignment characteristics between the principal strain rates and the iso-surfaces of C, expressed by $\cos \varphi_i^+$, as a function of C. The superscript $+$ denotes a quantity evaluated using $\nabla \boldsymbol{u}_s$ in (3.6). Symbols represent the conditional surface average for different cases as given in figure 19. In this figure, the progress variable is defined as $C = Y_{CO_2}$.

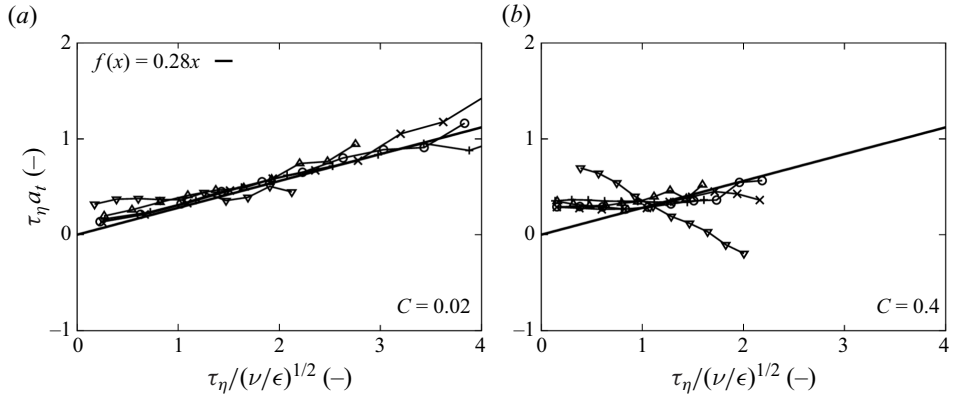

Figure 24. Normalized tangential strain rate $\tau_\eta a_t$ as a function of small-scale turbulence, expressed by $\tau_\eta/(\nu/\epsilon)^{1/2}$. Both variables are normalized with the Kolmogorov time evaluated in the unburned mixture, τ_η. Symbols represent the conditional surface average for different cases as given in figure 19. In this figure, the progress variable is defined as $C = Y_{CO_2}$.

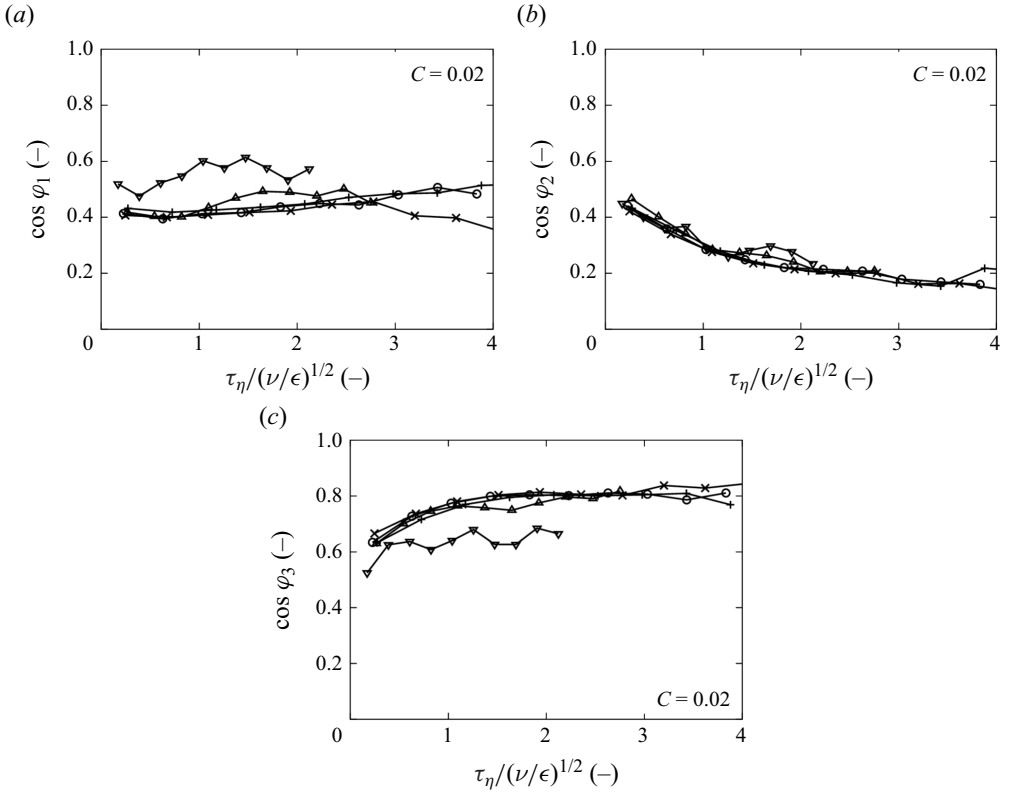

Figure 25. Alignment characteristics between the principal strain rates and the iso-surfaces of C, expressed by $\cos\varphi_i$, as a function of $\tau_\eta/(\nu/\epsilon)^{1/2}$ for $C = 0.02$ (negligible dilatation rate). Symbols represent the conditional surface average for different cases as given in figure 19. In this figure, the progress variable is defined as $C = Y_{CO_2}$.

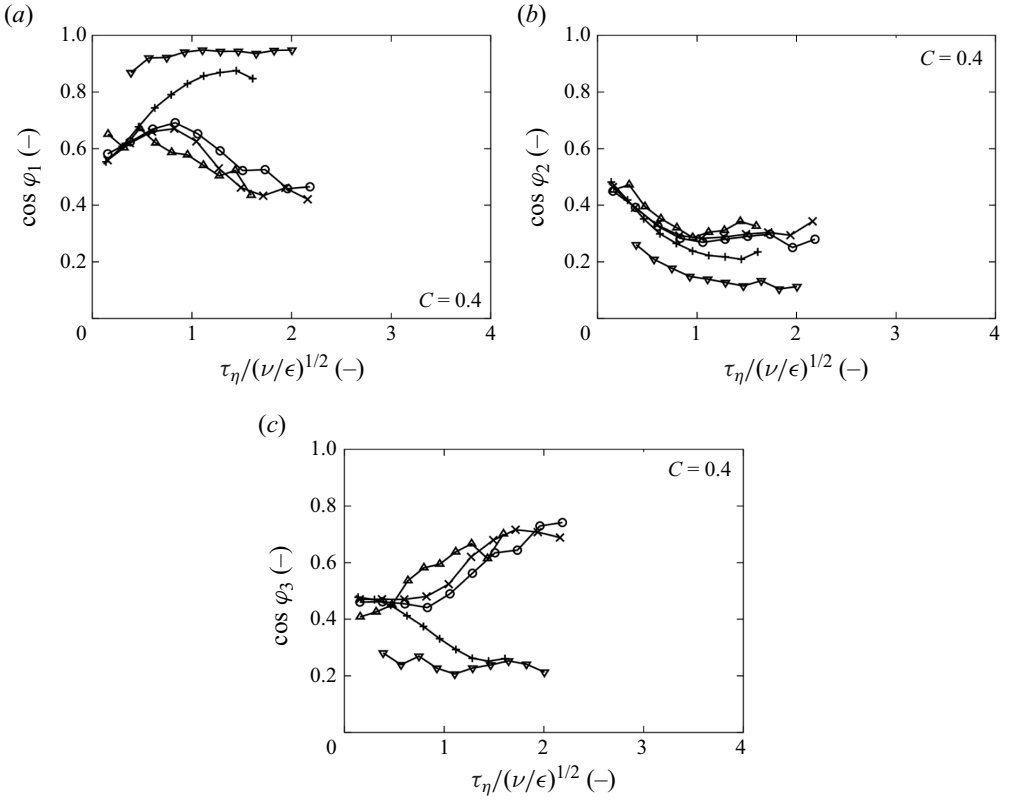

Figure 26. Alignment characteristics between the principal strain rates and the iso-surfaces of C, expressed by $\cos\varphi_i$, as a function of $\tau_\eta/(\nu/\epsilon)^{1/2}$ for regions with high dilatation rate. Symbols represent the conditional surface average for different cases as given in figure 19. In this figure, the progress variable is defined as $C = Y_{CO_2}$.

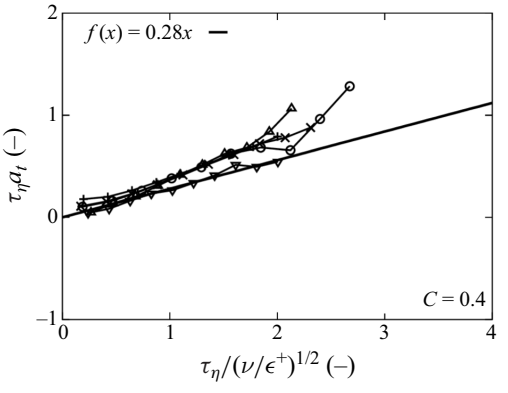

Figure 27. Normalized tangential strain rate $\tau_\eta a_t$ as a function of small-scale turbulence, expressed by $\tau_\eta/(\nu/\epsilon^+)^{1/2}$. The superscript + denotes a quantity evaluated using $\nabla \boldsymbol{u}_s$ in (3.6). Both variables are normalized with the Kolmogorov time evaluated in the unburned mixture, τ_η. Symbols represent the conditional surface average for different cases as given in figure 19. In this figure, the progress variable is defined as $C = Y_{CO_2}$.

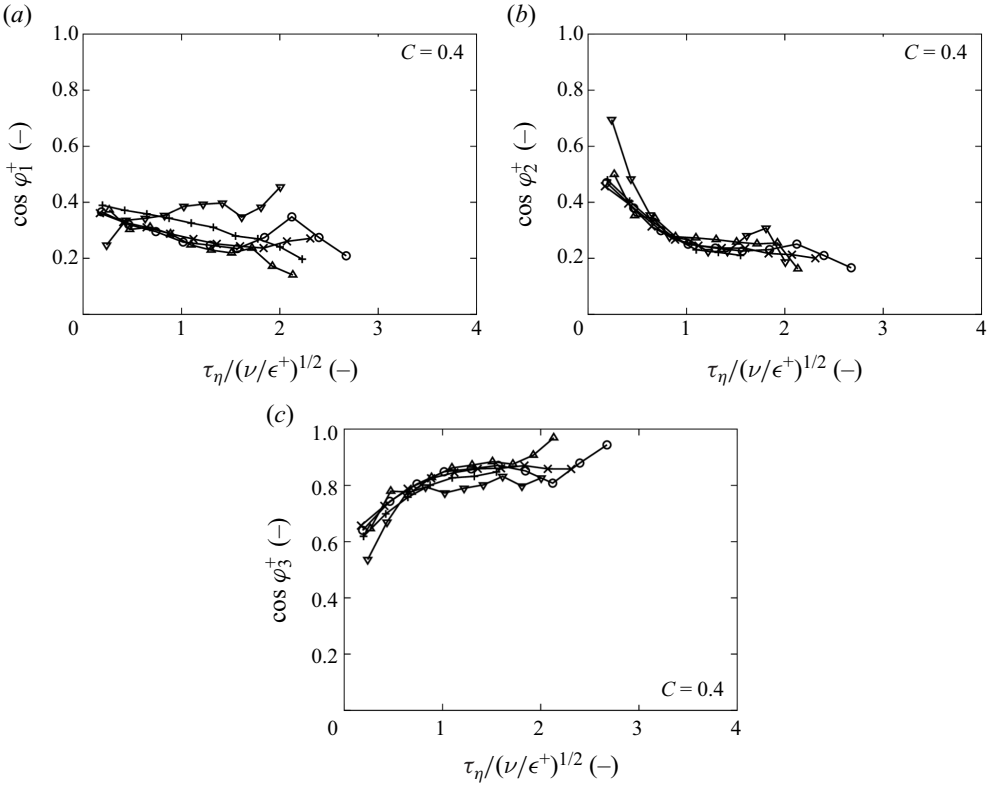

Figure 28. Alignment characteristics between the principal strain rates and the iso-surfaces of C, expressed by $\cos\varphi_i^+$, as a function of $\tau_\eta/(\nu/\epsilon^+)^{1/2}$. The superscript + denotes a quantity evaluated using $\nabla \boldsymbol{u}_s$ in (3.6). Symbols represent the conditional surface average for different cases as given in figure 19. In this figure, the progress variable is defined as $C = Y_{CO_2}$.

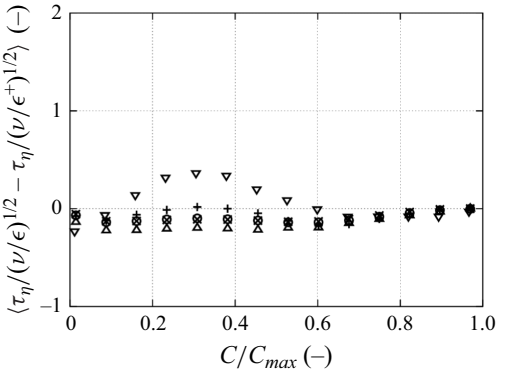

Figure 29. Effects of dilatation on the small-scale turbulence expressed by $\tau_\eta/(\nu/\epsilon)^{1/2}$. The superscript + denotes a quantity evaluated using $\nabla \boldsymbol{u}_s$ in (3.6). Symbols represent the conditional surface average for different cases as given in figure 19. In this figure, the progress variable is defined as $C = Y_{CO_2}$.

References

Aleiferis, P.G., Taylor, A.M.K.P., Ishii, K. & Urata, Y. 2004 The nature of early flame development in a lean-burn stratified-charge spark-ignition engine. *Combust. Flame* **136**, 283–302.

Ashurst, W.T., Kerstein, A.R., Kerr, R.M. & Gibson, C.H. 1987 Alignment of vorticity and scalar gradient with strain rate in simulated Navier–Stokes turbulence. *Phys. Fluids* **30**, 2343–2353.

Berger, L., Attili, A. & Pitsch, H. 2022 Synergistic interactions of thermodiffusive instabilities and turbulence in lean hydrogen flames. *Combust. Flame* **244**, 112254.

Blackburn, H.M., Mansour, N.N. & Cantwell, B.J. 1996 Topology of fine-scale motions in turbulent channel flow. *J. Fluid Mech.* **310**, 269–292.

Boger, M., Veynante, D., Boughanem, H. & Trouvé, A. 1998 Direct numerical simulation analysis of flame surface density concept for large eddy simulation of turbulent premixed combustion. *Symp. (Intl) Combust.* **27**, 917–925.

Bray, K.N.C. 1990 Studies of the turbulent burning velocity. *Proc. R. Soc. Lond.* A **431**, 315–335.

Bray, K.N.C. & Libby, P.A. 1994 Recent developments in the BML model of premixed turbulent combustion. In *Turbulent Reacting Flows* (ed. P.A. Libby & F.A. Williams), pp. 115–147. Academic.

Breda, M. & Buxton, O.R.H. 2019 Behaviour of small-scale turbulence in the turbulent/non-turbulent interface region of developing turbulent jets. *J. Fluid Mech.* **879**, 187–216.

Candel, S.M. & Poinsot, T.J. 1990 Flame stretch and the balance equation for the flame area. *Combust. Sci. Technol.* **70**, 1–15.

Cant, R.S., Pope, S.B. & Bray, K.N.C. 1991 Modelling of flamelet surface-to-volume ratio in turbulent premixed combustion. *Symp. (Intl) Combust.* **23**, 809–815.

Chakraborty, N. 2021 Influence of thermal expansion on fluid dynamics of turbulent premixed combustion and its modelling implications. *Flow Turbul. Combust.* **106**, 753–848.

Chakraborty, N., Klein, M. & Swaminathan, N. 2009 Effects of Lewis number on the reactive scalar gradient alignment with local strain rate in turbulent premixed flames. *Proc. Combust. Inst.* **32**, 1409–1417.

Chakraborty, N. & Swaminathan, N. 2007 Influence of the Damköhler number on turbulence-scalar interaction in premixed flames. I. Physical insight. *Phys. Fluids* **19**, 045103.

Chu, H., Berger, L., Grenga, T., Gauding, M., Cai, L. & Pitsch, H. 2023*a* Effects of turbulence on variations in early development of hydrogen and iso-octane flame kernels under engine conditions. *Combust. Flame* **255**, 112914.

Chu, H., Berger, L., Grenga, T., Wu, Z. & Pitsch, H. 2023*b* Effects of differential diffusion on hydrogen flame kernel development under engine conditions. *Proc. Combust. Inst.* **39** (2), 2129–2138.

Chu, H., Welch, C., Elmestikawy, H., Cao, S., Davidovic, M., Böhm, B., Dreizler, A. & Pitsch, H. 2022 A combined numerical and experimental investigation of cycle-to-cycle variations in an optically accessible spark-ignition engine. *Flow Turbul. Combust.* **110**, 3–29.

Desjardins, O., Blanquart, G., Balarac, G. & Pitsch, H. 2008 High order conservative finite difference scheme for variable density low Mach number turbulent flows. *J. Comput. Phys.* **227**, 7125–7159.

Dopazo, C., Cifuentes, L., Martin, J. & Jimenez, C. 2015 Strain rates normal to approaching iso-scalar surfaces in a turbulent premixed flame. *Combust. Flame* **162**, 1729–1736.

Duclos, J.M., Veynante, D. & Poinsot, T. 1993 A comparison of flamelet models for premixed turbulent combustion. *Combust. Flame* **95**, 101–117.

Elsinga, G.E. & Marusic, I. 2010 Universal aspects of small-scale motions in turbulence. *J. Fluid Mech.* **662**, 514–539.

Falgout, R.D. & Yang, U.M. 2002 hypre: a library of high performance preconditioners. In *Computational Science — ICCS 2002* (ed. P.M.A. Sloot, A.G. Hoekstra, C.J.K. Tan & J.J. Dongarra), pp. 632–641. Springer.

Falkenstein, T., Kang, S., Cai, L., Bode, M. & Pitsch, H. 2020*a* DNS study of the global heat release rate during early flame kernel development under engine conditions. *Combust. Flame* **213**, 455–466.

Falkenstein, T., Rezchikova, A., Langer, R., Bode, M., Kang, S. & Pitsch, H. 2020*b* The role of differential diffusion during early flame kernel development under engine conditions – part I: analysis of the heat-release-rate response. *Combust. Flame* **221**, 502–515.

Fontana, G. & Galloni, E. 2010 Experimental analysis of a spark-ignition engine using exhaust gas recycle at WOT operation. *Appl. Energy* **87**, 2187–2193.

Gauding, M., Thiesset, F., Varea, E. & Danaila, L. 2022 Structure of iso-scalar sets. *J. Fluid Mech.* **942**, A14.

Girimaji, S.S. & Pope, S.B. 1990 Material-element deformation in isotropic turbulence. *J. Fluid Mech.* **220**, 427–458.

Girimaji, S.S. & Pope, S.B. 1992 Propagating surfaces in isotropic turbulence. *J. Fluid Mech.* **234**, 247–277.

HAMLINGTON, P.E., POLUDNENKO, A.Y. & ORAN, E.S. 2011 Interactions between turbulence and flames in premixed reacting flows. *Phys. Fluids* **23** (12), 125111.

HAWKES, E.R & CANT, R.S 2001 Implications of a flame surface density approach to large eddy simulation of premixed turbulent combustion. *Combust. Flame* **126**, 1617–1629.

HAWKES, E.R., CHATAKONDA, O., KOLLA, H., KERSTEIN, A.R. & CHEN, J.H. 2012 A petascale direct numerical simulation study of the modelling of flame wrinkling for large-eddy simulations in intense turbulence. *Combust. Flame* **159**, 2690–2703.

HELMHOLTZ, H. 1858 Über Integrale der hydrodynamischen Gleichungen, welche den Wirbelbewegungen entsprechen. *J. Reine Angew. Math.* **1858**, 25–55.

HINDMARSH, A.C., BROWN, P.N., GRANT, K.E., LEE, S.L., SERBAN, R., SHUMAKER, D.E. & WOODWARD, C.S. 2005 Sundials: suite of nonlinear and differential/algebraic equation solvers. *ACM Trans. Math. Softw.* **31**, 363–396.

HIRSCHFELDER, J.O., CURTISS, C.F., BIRD, R.B. & MAYER, M.G. 1964 *Molecular Theory of Gases and Liquids*. Wiley.

JIANG, G. & SHU, C. 1996 Efficient implementation of weighted ENO schemes. *J. Comput. Phys.* **126**, 202–228.

JILAKARA, S., VAITHIANATHAN, J.V., NATARAJAN, S., RAMAKRISHNAN, V.R., SUBASH, G.P., ABRAHAM, M., UNNI, J.K. & DAS, L.M. 2015 An experimental study of turbocharged hydrogen fuelled internal combustion engine. *SAE Intl J. Engines* **8**, 314–325.

JOULIN, G. & MITANI, T. 1981 Linear stability analysis of two-reactant flames. *Combust. Flame* **40**, 235–246.

JUNG, D., SASAKI, K. & IIDA, N. 2017 Effects of increased spark discharge energy and enhanced in-cylinder turbulence level on lean limits and cycle-to-cycle variations of combustion for SI engine operation. *Appl. Energy* **205**, 1467–1477.

KARGUL, J., STUHLDREHER, M., BARBA, D., SCHENK, C., BOHAC, S., MCDONALD, J., DEKRAKER, P. & ALDEN, J. 2019 Benchmarking a 2018 Toyota Camry 2.5-Liter Atkinson Cycle Engine with Cooled-EGR. *SAE Intl J. Adv. Curr. Prac. Mobility* **1**, 601–638.

KARVOUNTZIS-KONTAKIOTIS, A., DIMARATOS, A., NTZIACHRISTOS, L. & SAMARAS, Z. 2017 Exploring the stochastic and deterministic aspects of cyclic emission variability on a high speed spark-ignition engine. *Energy* **118**, 68–76.

KERR, R.M. 1985 Higher-order derivative correlations and the alignment of small-scale structures in isotropic numerical turbulence. *J. Fluid Mech.* **153**, 31–58.

KIM, S.H. & PITSCH, H. 2007 Scalar gradient and small-scale structure in turbulent premixed combustion. *Phys. Fluids* **19**, 115104.

KONNOV, A.A. 2019 Yet another kinetic mechanism for hydrogen combustion. *Combust. Flame* **203**, 14–22.

KRISMAN, A., MEAGHER, P., ZHAO, X., PARK, J., LU, T. & CHEN, J.H. 2021 A direct numerical simulation of Jet A flame kernel quenching. *Combust. Flame* **225**, 349–363.

KULKARNI, T. & BISETTI, F. 2021 Evolution and scaling of the peak flame surface density in spherical turbulent premixed flames subjected to decaying isotropic turbulence. *Proc. Combust. Inst.* **38**, 2817–2824.

KULKARNI, T., BUTTAY, R., KASBAOUI, M.H., ATTILI, A. & BISETTI, F. 2021 Reynolds number scaling of burning rates in spherical turbulent premixed flames. *J. Fluid Mech.* **906**, A2.

LUCA, S., ATTILI, A., LO SCHIAVO, E., CRETA, F. & BISETTI, F. 2019 On the statistics of flame stretch in turbulent premixed jet flames in the thin reaction zone regime at varying Reynolds number. *Proc. Combust. Inst.* **37**, 2451–2459.

LUSZCZ, P., TAKEUCHI, K., PFEILMAIER, P., GERHARDT, M., ADOMEIT, P., BRUNN, A., KUPIEK, C. & FRANZKE, B. 2018 Homogeneous lean burn engine combustion system development – concept study. In *18. Internationales Stuttgarter Symposium* (ed. M. Bargende, H.-C. Reuss & J. Wiedermann), pp. 205–223. Springer.

MÜLLER, B. 1998 Low-Mach-number asymptotics of the Navier–Stokes equations. *J. Engng Maths* **34**, 97–109.

PANICKACHERIL JOHN, J., DONZIS, D.A. & SREENIVASAN, K.R. 2021 Does dissipative anomaly hold for compressible turbulence? *J. Fluid Mech.* **920**, A20.

PETERS, N. 2001 *Turbulent Combustion*. Cambridge University Press.

PITSCH, H., PETERS, N. & SESHADRI, K. 1996 Numerical and asymptotic studies of the structure of premixed iso-octane flames. *Symp. (Intl) Combust.* **26**, 763–771.

PRAUTZSCH, H. & BOEHM, W. 2018 *Geometric Concepts for Geometric Design*. AK Peters/CRC.

RUTLAND, C.J. & TROUVÉ, A. 1993 Direct simulations of premixed turbulent flames with nonunity Lewis numbers. *Combust. Flame* **94**, 41–57.

SABELNIKOV, V.A., LIPATNIKOV, A.N., NIKITIN, N.V., HERNÁNDEZ PÉREZ, F.E. & IM, H.G. 2023 Backscatter of scalar variance in turbulent premixed flames. *J. Fluid Mech.* **960**, R2.

SANKARAN, R., HAWKES, E.R., CHEN, J.H., LU, T. & LAW, C.K. 2007 Structure of a spatially developing turbulent lean methane–air bunsen flame. *Proc. Combust. Inst.* **31** (1), 1291–1298.

SANKARAN, R., HAWKES, E.R., YOO, C.S. & CHEN, J.H. 2015 Response of flame thickness and propagation speed under intense turbulence in spatially developing lean premixed methane–air jet flames. *Combust. Flame* **162** (9), 3294–3306.

SCHIFFMANN, P., REUSS, D.L. & SICK, V. 2018 Empirical investigation of spark-ignited flame-initiation cycle-to-cycle variability in a homogeneous charge reciprocating engine. *Intl J. Engine Res.* **19**, 491–508.

SCHLUP, J. & BLANQUART, G. 2018 Validation of a mixture-averaged thermal diffusion model for premixed lean hydrogen flames. *Combust. Theor. Model.* **22**, 264–290.

SORIA, J., SONDERGAARD, R., CANTWELL, B.J., CHONG, M.S. & PERRY, A.E. 1994 A study of the fine-scale motions of incompressible time-developing mixing layers. *Phys. Fluids* **6**, 871–884.

STRANG, G. 1968 On the construction and comparison of difference schemes. *SIAM J. Numer. Anal.* **5**, 506–517.

SWAMINATHAN, N. & GROUT, R.W. 2006 Interaction of turbulence and scalar fields in premixed flames. *Phys. Fluids* **18**, 045102.

TANG, X., KABAT, D.M., NATKIN, R.J., STOCKHAUSEN, W.F. & HEFFEL, J. 2002 Ford P2000 hydrogen engine dynamometer development. *SAE Trans.* **111**, 631–642.

THIESSET, F., HALTER, F., BARIKI, C., LAPEYRE, C., CHAUVEAU, C., GÖKALP, I., SELLE, L. & POINSOT, T. 2017 Isolating strain and curvature effects in premixed flame/vortex interactions. *J. Fluid Mech.* **831**, 618–654.

VERHELST, S., MAESSCHALCK, P., ROMBAUT, N. & SIERENS, R. 2009 Increasing the power output of hydrogen internal combustion engines by means of supercharging and exhaust gas recirculation. *Intl J. Hydrogen Energy* **34**, 4406–4412.

WANG, H., HAWKES, E.R. & CHEN, J.H. 2016 Turbulence-flame interactions in DNS of a laboratory high Karlovitz premixed turbulent jet flame. *Phys. Fluids* **28** (9), 095107.

WANG, H., HAWKES, E.R., CHEN, J.H., ZHOU, B., LI, Z. & ALDÉN, M. 2017 Direct numerical simulations of a high Karlovitz number laboratory premixed jet flame – an analysis of flame stretch and flame thickening. *J. Fluid Mech.* **815**, 511–536.

WANG, J., WAN, M., CHEN, S. & CHEN, S. 2018 Kinetic energy transfer in compressible isotropic turbulence. *J. Fluid Mech.* **841**, 581–613.

WARHAFT, Z. 2000 Passive scalars in turbulent flows. *Annu. Rev. Fluid Mech.* **32**, 203–240.

YE, C., SUN, Z., CUI, M., LI, X., HUNG, D. & XU, M. 2021 Ultra-lean limit extension for gasoline direct injection engine application via high energy ignition and flash boiling atomization. *Proc. Combust. Inst.* **38**, 5829–5838.

YEUNG, P.K., GIRIMAJI, S.S. & POPE, S.B. 1990 Straining and scalar dissipation on material surfaces in turbulence: implications for flamelets. *Combust. Flame* **79**, 340–365.

YOUNG, M.B. 1981 Cyclic dispersion in the homogeneous-charge spark-ignition engine – a literature survey. *SAE Trans.* **90**, 49–73.

ZENG, W., KEUM, S., KUO, T. & SICK, V. 2019 Role of large scale flow features on cycle-to-cycle variations of spark-ignited flame-initiation and its transition to turbulent combustion. *Proc. Combust. Inst.* **37**, 4945–4953.

ZHENG, Q., WANG, J., MAHBUB ALAM, MD., NOACK, B.R., LI, H. & CHEN, S. 2021 Transfer of internal energy fluctuation in compressible isotropic turbulence with vibrational non-equilibrium. *J. Fluid Mech.* **919**, A26.

ZHENG, Q., YANG, Y., WANG, J. & CHEN, S. 2022 Enstrophy production and flow topology in compressible isotropic turbulence with vibrational non-equilibrium. *J. Fluid Mech.* **950**, A21.

ZHOU, Z., HERNÁNDEZ-PÉREZ, F.E., SHOSHIN, Y., VAN OIJEN, J.A. & DE GOEY, L.P.H. 2017 Effect of soret diffusion on lean hydrogen/air flames at normal and elevated pressure and temperature. *Combust. Theor. Model.* **21**, 879–896.